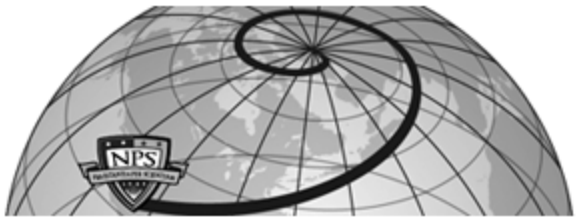

NAVAL POSTGRADUATE SCHOOL

MONTEREY, CALIFORNIA

THESIS

SPATIAL MAPPING OF THE MOBILITY-LIFETIME ($\mu\tau$) PRODUCT IN CADMIUM ZINC TELLURIDE NUCLEAR RADIATION DETECTORS USING TRANSPORT IMAGING

by

Peter J. Young Jr.

June 2013

Thesis Advisor: Nancy Haegel
Co-Advisor: Chris Frenzen

THIS PAGE INTENTIONALLY LEFT BLANK

REPORT DOCUMENTATION PAGE	Form Approved OMB No. 0704-0188

1. AGENCY USE ONLY *(Leave blank)*	2. REPORT DATE	3. REPORT TYPE AND DATES COVERED
	June 2013	Thesis

4. TITLE AND SUBTITLE: SPATIAL MAPPING OF THE MOBILITY-LIFETIME ($\mu\tau$) PRODUCT IN CADMIUM ZINC TELLURIDE NUCLEAR RADIATION DETECTORS USING TRANSPORT IMAGING	5. FUNDING NUMBERS V7C6E
6. AUTHOR(S): Peter J. Young Jr.	
7. PERFORMING ORGANIZATION NAME(S) AND ADDRESS(ES) Naval Postgraduate School Monterey, CA 93943-5000	8. PERFORMING ORGANIZATION REPORT NUMBER
9. SPONSORING / MONITORING AGENCY NAME(S) AND ADDRESS(ES) Department of Homeland Security (DHS)/Domestic Nuclear Detection Office	10. SPONSORING / MONITORING AGENCY REPORT NUMBER

11. SUPPLEMENTARY NOTES: The views expressed in this thesis are those of the author and do not reflect the official policy or position of the Department of Defense or the U.S. government. I.R.P. Protocol number N/A.

12a. DISTRIBUTION / AVAILABILITY STATEMENT	12b. DISTRIBUTION CODE
Approved for public release; distribution is unlimited	A

13. ABSTRACT (maximum 200 words)

Cadmium zinc telluride ($Cd_{1-x}Zn_xTe$) is an important material for room temperature nuclear radiation detectors due to its high stopping power for gamma rays combined with its good electron transport. However, CdZnTe crystals are susceptible to growth defects such as grain boundaries, twin boundaries, and tellurium (Te) inclusions which can compromise desirable energy resolution and electron/hole charge collection properties. The presence of these defects ultimately degrades the effectiveness of the nuclear radiation detector material. The ability to map electron and hole transport properties at high spatial resolution can provide new insight into the roles of individual defects.

Experimentally, this study employs high-resolution (< 5μm) transport imaging to explore the effect of localized crystal defects on the spatial variation of carrier transport properties. The ambipolar diffusion length (L_d) and associated free carrier mobility-lifetime (μτ) product are determined by imaging the recombination luminescence from carriers generated by an electron beam. Localized defects often are marked by regions of low intensity luminescence. At the same time, we observe increasing ambipolar diffusion length in the region immediately surrounding the defects. One explanation is that the gettering of point defects, such as interstitials and vacancies, associated with the formation of microscopic precipitates results in localized increases in the μτ product. Initial results indicate that these variations occur over a region extending ~ 10 μm from the edge of the inclusion.

Mathematically, this study employs the minority carrier diffusion equation to model the 3D diffusion of free charge carriers away from a point source. A non-linear least squares program using exact methods and asymptotic expansion methods is then used to fit this model to transport data imagery. The ambipolar diffusion length (L_d) and associated free carrier mobility-lifetime (μτ) is then determined from the scanned portion of the sample. A plot of diffusion length versus position is also revealed, which depicts the sample's spatial variation of carrier transport properties.

.

14. SUBJECT TERMS: Transport Imaging, Cathodoluminescence, Mobility-Lifetime ($\mu\tau$) Product, Cadmium Zinc Telluride, CZT, Spatial Variation	15. NUMBER OF PAGES 95
	16. PRICE CODE

17. SECURITY CLASSIFICATION OF REPORT	18. SECURITY CLASSIFICATION OF THIS PAGE	19. SECURITY CLASSIFICATION OF ABSTRACT	20. LIMITATION OF ABSTRACT
Unclassified	Unclassified	Unclassified	UU

NSN 7540-01-280-5500 Standard Form 298 (Rev. 2-89) Prescribed by ANSI Std. 239-18

THIS PAGE INTENTIONALLY LEFT BLANK

Approved for public release; distribution is unlimited

SPATIAL MAPPING OF THE MOBILITY-LIFETIME ($\mu\tau$) PRODUCT IN CADMIUM ZINC TELLURIDE NUCLEAR RADIATION DETECTORS USING TRANSPORT IMAGING

Peter J. Young Jr.
Major, United States Army
B.S., United States Military Academy, 2003

Submitted in partial fulfillment of the
requirements for the degree of

MASTER OF SCIENCE IN PHYSICS
AND
MASTER OF SCIENCE IN APPLIED MATHEMATICS

from the

NAVAL POSTGRADUATESCHOOL

June 2013

Author: Peter J. Young Jr.

Approved by: Nancy Haegel
Thesis Co-Advisor

Chris Frenzen
Thesis Co-Advisor

Andres Larraza
Chair, Department of Physics

THIS PAGE INTENTIONALLY LEFT BLANK

ABSTRACT

Cadmium zinc telluride ($Cd_{1-x}Zn_xTe$) is an important material for room temperature nuclear radiation detectors due to its high stopping power for gamma rays combined with its good electron transport. However, CdZnTe crystals are susceptible to growth defects such as grain boundaries, twin boundaries, and tellurium (Te) inclusions which can compromise desirable energy resolution and electron/hole charge collection properties. The presence of these defects ultimately degrades the effectiveness of the nuclear radiation detector material. The ability to map electron and hole transport properties at high spatial resolution can provide new insight into the roles of individual defects.

Experimentally, this study employs high-resolution (< 5μm) transport imaging to explore the effect of localized crystal defects on the spatial variation of carrier transport properties. The ambipolar diffusion length (L_d) and associated free carrier mobility-lifetime ($\mu\tau$) product are determined by imaging the recombination luminescence from carriers generated by an electron beam. Localized defects often are marked by regions of low intensity luminescence. At the same time, we observe increasing ambipolar diffusion length in the region immediately surrounding the defects. One explanation is that the gettering of point defects, such as interstitials and vacancies, associated with the formation of microscopic precipitates results in localized increases in the $\mu\tau$ product. Initial results indicate that these variations occur over a region extending ~ 10 μm from the edge of the inclusion.

Mathematically, this study employs the minority carrier diffusion equation to model the 3D diffusion of free charge carriers away from a point source. A non-linear least squares program using exact methods and asymptotic expansion methods is then used to fit this model to transport data imagery. The ambipolar diffusion length (L_d) and associated free carrier mobility-lifetime ($\mu\tau$) is then determined from the scanned portion of the sample. A plot of diffusion length versus position is also revealed, which depicts the sample's spatial variation of carrier transport properties.

THIS PAGE INTENTIONALLY LEFT BLANK

TABLE OF CONTENTS

THIS PAGE INTENTIONALLY LEFT BLANK

LIST OF FIGURES

THIS PAGE INTENTIONALLY LEFT BLANK

LIST OF TABLES

THIS PAGE INTENTIONALLY LEFT BLANK

LIST OF ACRONYMS AND ABBREVIATIONS

CL	Cathodoluminescence
CCD	Charge Coupled Device
CdTe	Cadmium Telluride
CZT	Cadmium Zinc Telluride
EDS	Energy Dispersive X-ray Spectroscopy
FWHM	Full Width at Half Maximum
SEM	Scanning Electron Microscope
FIB	Focused Ion Beam Milling
EDS	Energy Dispersive X-ray Spectroscopy

THIS PAGE INTENTIONALLY LEFT BLANK

ACKNOWLEDGMENTS

This work was supported by the DNDO Academic Research Initiative Grant NSF/ARI 083007.

I would like to thank REDLEN Technologies and Brookhaven National Laboratory for providing samples of CdZnTe for the transport imaging experiments involved in this thesis.

I would also like to thank my advisor, Prof. Nancy Haegel, for welcoming me into her research group, providing mentorship and patience during our transport imaging experiments, and motivating me to pursue a career in materials science. Thanks also to Prof. Chris Frenzen and Prof. Clyde Scandrett for helping me develop an asymptotic expansion improvement to the three-dimensional transport imaging mathematical model and non-linear least squares fitting algorithm.

Thanks to Kevin Blaine for developing the initial three-dimensional mathematical model behind transport imaging and granting me permission to continue his research. Thanks also to David Phillips for sharing his initial findings regarding CdZnTe defects and the diffusion length trends observed in their immediate vicinity.

Thanks to Kevin Tang for working diligently during his summer internship to develop an independent transport imaging mathematical model to verify David's and Kevin's findings on diffusion length trends near crystal defects.

A special thanks to Prof. Sarath Menon for volunteering his time and his department's microscope to perform energy-dispersive x-ray spectroscopy and focused ion beam milling procedures to help us investigate crystal defects within our samples.

Thanks to Fritz Schultes for his frequent road trips to visit our collaborators at the University of California Berkeley and acquire radiation-damaged samples to test our mathematical model and verify our findings.

Finally, I would like to thank to my wife, Patricia, for supporting my goals and raising our family while I spent extended hours at school performing experiments to complete this thesis.

I. INTRODUCTION

A. THE NUCLEAR THREAT AND THE DETECTOR PROBLEM

Tactical nuclear weapons pose a significant threat to national security. Their low radiation signature helps them avoid detection, while their portability makes them easily transportable across porous borders and past inattentive border agents. One can only imagine a scenario wherein a tactical nuclear weapon would be detonated within a highly-populated area or against key infrastructure. Such a terrible event has yet to happen, yet there is no denying this as an ideal terrorist success story. For this and many other reasons, tactical nuclear weapons are the non-state actor's weapon of choice. Foreign Policy magazine reports, "Al Qaeda's leaders yearn to acquire and use weapons of mass destruction against the United States; if they acquired a nuclear bomb, they would not hesitate to use it" [1].

The events of 9/11 inspired significant improvements in screening procedures performed at seaports, airports, railways, and roadways, yet the low-resolution radiation detectors employed there often cannot resolve kitty litter from highly-enriched uranium [2]. Moreover, these low-resolution detectors may fail to detect legitimate gamma radiation sources such as those employed in a tactical nuclear weapon. This problem has inspired scientists within the detector community to research higher-resolution detector materials that can both operate at room temperature and be capable of positively-identifying such threats.

Among many other materials of promise, Cadmium Zinc Telluride (CZT or CdZnTe) has demonstrated its efficacy as a gamma ray detector material, though there is still much to learn about its inherent structural defects. CdZnTe is currently used in a range of medical imaging and security systems, but more work is needed to make it cost-effective for widespread use in the global nuclear detection architecture.

B. DETECTOR THEORY

In the most simplified case, semiconductor nuclear radiation detectors consist of detector material connected to an electronic circuit by means of electrodes attached to either side of the material. As incident radiation is absorbed within the detector material, electron-hole pairs are generated in the conduction and valence bands respectively, at a rate proportional to the incident radiation intensity. Under the influence of an electrical field, these electrons and holes migrate to their respective electrodes, where they are collected and interpreted by the attached electronic circuit as incident radiation intensity.

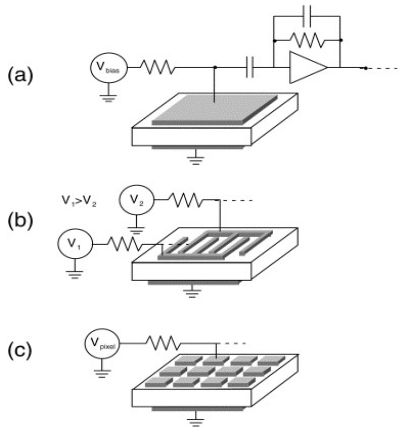

Figure 1. Schematic diagram of three basic nuclear detection geometries: (a) single element planar detector; co-planar grid detector; (c) pixellated detector for imaging applications. From [3]

Detector resolution is heavily dependent on the quality of semiconductor or scintillator material employed. The more uniformly the detector material collects charge, the more electron-hole pairs make it to the detector contacts to reflect the intensity and wavelength of incident radiation. While scintillators and semiconductors differ in their collection method of photons or electron/hole pairs respectively, the end result is the same: incident radiation produces an electrical response which translates to an intensity reading on the detector's readout meter. Since high-resolution detector materials are the focus of this thesis, only research on semiconductor materials will be discussed.

The resolution R [%] of a gamma-ray detector is commonly defined in terms of its energy peak full-width at half maximum (FWHM, or ΔE) [eV] divided by the centroid of the energy peak E_0 [eV] [4].

$$R = \frac{FWHM}{E_0} = \frac{\Delta E}{E_0}. \tag{1}$$

An idealized detector response and FWHM is shown graphically in Figure 2.

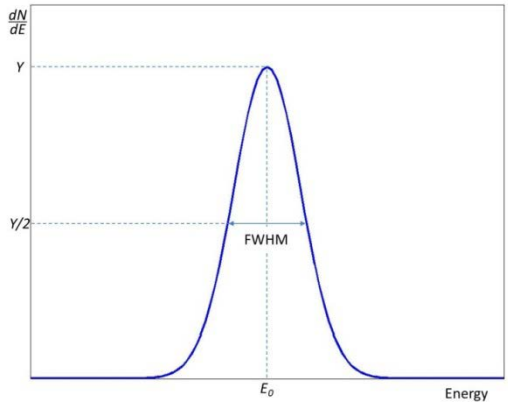

Figure 2. Simulated gamma-ray peak with FWHM and centroid energy peak E_0 [4].

A narrow FWHM results in a sharp energy peak and thus, a high-resolution measurement capability for the detector. Conversely, a wide FWHM translates into a dull energy peak and thus, a low-resolution capability. The FWHM ΔE is narrowed or widened depending on the magnitude of three factors: inherent statistical variation of the electric signal measured at the detector's contacts (Fano noise ΔE_F), random electron-hole interactions in the absence of incident gamma rays (electronic noise ΔE_E), and noise (phonons) generated as charge carriers recombine at crystal defects instead of migrating to the detector electrodes (carrier-hindered noise ΔE_C) [4]. The equation for FWHM is given by

$$\Delta E = \sqrt{\left(\Delta E_F\right)^2 + \left(\Delta E_E\right)^2 + \left(\Delta E_C\right)^2}. \tag{2}$$

High concentrations of crystal defects render a detector material prone to large amounts of carrier-hindered noise, which conceivably dominates other noise sources and widens a detector's FWHM as seen in Equation (2).

To further explore the factor of incomplete charge collection, one may consider a detector's charge collection efficiency (CCE) [4]. CCE is a ratio of the total charge Q [C] measured on the detector contacts divided by the amount of charge Q_0 [C] created as electron/hole pairs are generated by an incident gamma-ray.

$$CCE = \frac{Q}{Q_0}. \tag{3}$$

In a perfect detector with no crystal defects, all electron/hole pairs generated by incident gamma rays arrive at the detector contacts, reflecting a CCE ratio of 1, a carrier-hindered noise magnitude of zero, a, narrow FWHM, and a sharp detector resolution peak. In practice, however, CCE is degraded by material factors such as carrier diffusion, carrier trapping, and spatial variations in charge collection capability [4]. All three material factors broaden the detector's resolution peak, ultimately making it more difficult for detector electronics to precisely identify radiation wavelength and intensity. This thesis seeks to examine these spatial variations in the vicinity of CZT crystal defects that affect detector resolution.

C. DETECTOR MATERIALS RESEARCH

Ideal nuclear radiation detector materials have high average atomic number (Z), high bulk resistivity, large bandgap, good photoconductivity, low leakage current, and sufficient electron/hole transport to allow for carrier transport and collection of the EHPs at the contacts [5]. High Z values translate to the "stopping power" of the detector, or how effective the material absorbs gamma radiation. Higher Z values are desirable, as they allow for thinner detector materials to absorb a similar amount of gamma radiation as those of thicker materials with lower Z values. Large bandgap materials are also desirable, as they have less thermal carrier generation which promotes higher signal-to-noise ratios, allowing for higher detector resolution at room temperature. Smaller bandgap materials have higher thermal carrier generation and therefore must be

externally cooled to achieve comparable sensitivity and resolution. A comparison of three popular gamma ray detector materials is given below in Table 1.

Material	Average Atomic Number	Bandgap	Operating Temp
Germanium (Ge)	$Z_{Ge} = 32$	$E_g = 0.67\ eV$	$77\ K$
Thallium Bromide (TlBr)	$Z_{Tl} = 81\ \ (50\%)$ $Z_{Br} = 35\ \ (50\%)$ $\Big\} Z_{avg} = 58$	$E_g = 3.00\ eV$	$295\ K$
Cadmium Zinc Telluride ($Cd_{1-x}Zn_xTe$) $0.1 \le x \le 0.2$	$Z_{Cd} = 48\ \ (42.5\%)$ $Z_{Zn} = 30\ \ (7.5\%)$ $Z_{Te} = 52\ \ (50\%)$ $\Big\} Z_{avg} = 49$	$E_g = 1.57\ eV$	$295\ K$

Table 1. Popular nuclear radiation detector materials.

The highly-pure germanium detector mentioned in Table 1 has a relatively low atomic number and a small bandgap, which requires the detector to be thicker and cooled to liquid nitrogen temperatures to achieve a suitable signal-to-noise ratio for gamma radiation detection. Since these cooling methods are expensive and not widely available, HPG detectors are not feasible at many border-crossings or inspection areas. Thallium Bromide (TlBr) and Cadmium Zinc Telluride (CdZnTe) materials, by contrast, have higher average atomic numbers and larger bandgaps than Germanium, so they can operate effectively at room temperature without the need for external cooling. For these reasons, both materials are of great interest to the detector community.

Unfortunately, CZT bulk semiconductors are prone to defects as they are grown. These defects—grain boundaries, twin boundaries, precipitates and inclusions—are known to degrade the crystal's electron/hole transport properties, which compromises carrier lifetime and ultimately degrades energy resolution [6]. Non-radiative recombination (or trapping) is known to occur at these defects, preventing charge carriers from otherwise arriving to the contacts unhindered. Lost electron/hole pairs compromise the detector's ability to accurately measure the magnitude of incident radiation. The energy band diagram depicted in Figure 3 below helps to illustrate this phenomenon.

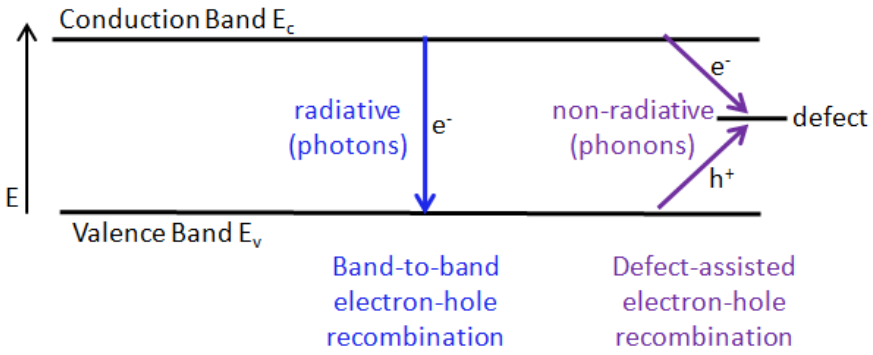

Figure 3. Energy band diagram for radiative and non-radiative EHP recombination.

CdZnTe crystals are typically grown via the High-Pressure Bridgeman (HPB) method, which immerses the crystal in a high-pressure environment of inert gas (such as argon) as it is grown [6]. This high-pressure gas prevents newly-grown charge material from evaporating as it is formed. As the material cools to room temperature, though, tellurium and/or cadmium can precipitate out of the $Cd_{1-x}Zn_xTe$ lattice and nucleate at low-energy locations within the crystal, creating sites for non-radiative recombination [6].

It has been historically difficult to trace and characterize defects within CZT crystals, as they tend to exist at the level of parts per billion by weight (ppbw) [5]. A variety of imaging methods have been employed to study crystal defect distribution and determine their effect on the bulk material's overall charge transport qualities. While these techniques seek to extract CZT's macroscopic charge transport qualities via charge collection measurements at detector contacts with an applied electric field, these methods fail to provide the sub-5μm level of resolution necessary to spatially-map charge transport around single defects of sub-micron size.

Transport imaging is a characterization method under development at the Naval Postgraduate School that employs a contact-free, non-destructive, optical method of determining a semiconductor's mobility-lifetime ($\mu\tau$) product at the 2μm-level of resolution. Instead of averaging charge transport variations over the entire detector area between the contacts, transport imaging maps EHP diffusion and recombination in focused areas by mapping the associated recombination luminescence. This thesis describes the first detailed study of transport surrounding single defects in CZT.

D. THE MOBILITY-LIFETIME PRODUCT

The mobility-lifetime ($\mu\tau$) product [m^2/V] is an important metric which determines how far electrons or holes travel within a semiconductor under the influence of an electric field. The mobility-lifetime product is derived from Einstein's relation (4) and the diffusion length equation (5), where D is the diffusion coefficient [m^2/s], k is Boltzmann's constant [J/K], T is the absolute temperature [K], e is the elementary electron charge [C], μ is the carrier mobility [m^2/Vs], L_d is the diffusion length [m], and τ is the carrier lifetime [s].

$$D = \frac{kT}{e}\mu \,. \tag{4}$$

$$L_d = \sqrt{D\tau} \,. \tag{5}$$

A combination of Einstein's relation and the diffusion length equation yields the mobility-lifetime equation (6), which relates diffusion length to the $\mu\tau$ product.

$$L_d = \sqrt{\frac{kT}{e}\mu\tau} \,. \tag{6}$$

Diffusion length L_d depends on the mobility μ and lifetime τ material properties. Equation (6) shows how variations in the $\mu\tau$ product can cause consequent variations in diffusion length L_d. Since variations in $\mu\tau$ ultimately compromise detector resolution, variations in L_d can be studied to reveal important charge transport qualities about the detector material.

E. RESEARCH OBJECTIVES AND GOALS

The broad objective of this research is to employ a 3D carrier diffusion model in CZT to demonstrate the application of transport imaging as a micro-analysis tool for characterizing charge transport properties in bulk semiconductors for nuclear radiation detection. The specific goals of this research are to:

- Map Ld variations near CZT crystal defects at the 2μm resolution level using transport imaging

- Investigate defect geometry at or beneath the sample surface with Cathodoluminescence (CL) imaging
- Locate and investigate defects beneath the sample surface using Focused Ion Beam (FIB) milling.
- Determine defect composition using Energy-Dispersive X-Ray Spectroscopy (EDS)
- Asymptotically-expand the 3D transport imaging mathematical model in order to allow for multiple surface recombination velocity (S) values from zero to ∞.
- Design and test an independent nonlinear least-squares algorithm to fit the asymptotically-expanded mathematical model to image data captured during transport imaging.

II. TRANSPORT IMAGING

A. OVERVIEW

Transport imaging is a method of spatially mapping the recombination of minority carriers or EHPs in luminescent semiconductors. It works by applying a focused electron beam of specified acceleration voltage [eV] and probe current [A] to a sample, which creates a surplus of cascading EHPs in a bulbous interaction volume [$EHPs/cm^3$] beneath the sample surface at a magnitude dependent on the incident beam intensity and the sample's average atomic weight (Z). These EHPs are created primarily through photoelectric, Compton, and pair production interactions.

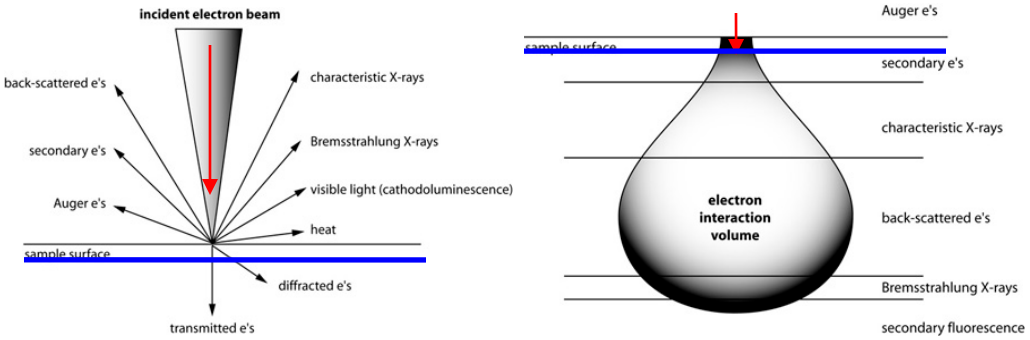

Figure 4. Electron beam interaction with sample surface. After [7]

These EHPs diffuse outward and recombine radiatively or non-radiatively, depending on the presence or absence of crystal defects in the diffusion path. EHPs which undergo radiative recombination release photons on the order of the bandgap energy E_g [eV], while EHP which undergo non-radiative recombination release phonons on the order of defect gap E_{defect} [eV] that contribute to carrier-hindered noise ΔE_C. A charge-coupled device (CCD) captures the spatially-varying pattern of radiatively-recombining EHPs in an image, which is then evaluated using a mathematical model to determine the material's diffusion length L_d and the mobility-lifetime ($\mu\tau$) product as a function of position on the sample. The formula for determining the CCD cutoff

wavelength (7) uses Planck's constant h [J], the speed of light c [m/s], the elementary charge e [C] and the bandgap energy E_g [eV].

$$\lambda_{CCD} = \frac{hc}{eE_g}. \tag{7}$$

Pristine areas of the sample that uniformly collect and distribute charge will appear uniformly bright in cathodoluminescence imaging, while defective areas of a sample will display more spatial variation, generally appearing brighter in some areas and darker near defective regions. These spatial variations can be studied to determine charge transport qualities in areas immediately surrounding crystal defects.

B. EXPERIMENTAL SETUP

Our transport imaging for bulk materials employs a JEOL 840A scanning electron microscope (SEM) equipped with an adjustable optical microscope and an externally-attached CCD array camera (Figure 5).

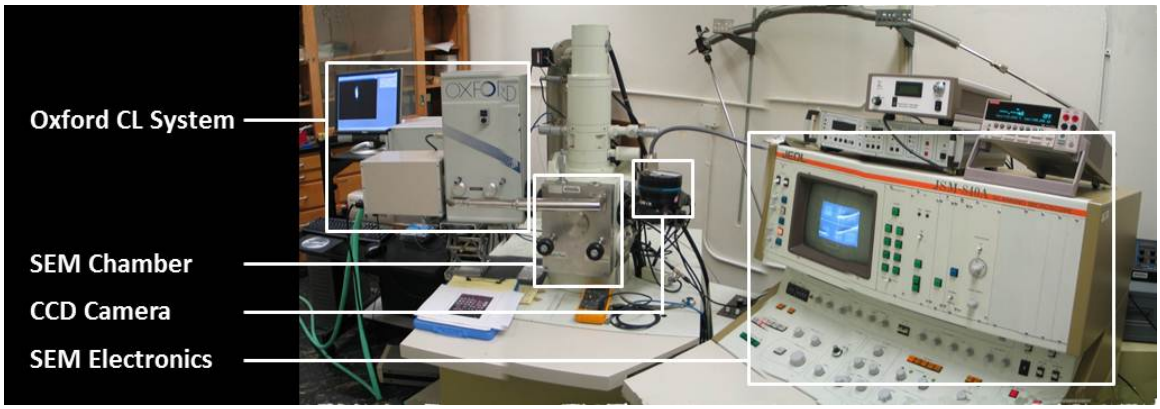

Figure 5. JEOL 840A setup for transport imaging. From [4]

The objective lens of the adjustable optical microscope is inserted into the SEM's vacuum chamber using a retractable arm in order to capture spatially-varying EHP recombination luminescence patterns produced as the electron beam bombards the sample. (Figure 6)

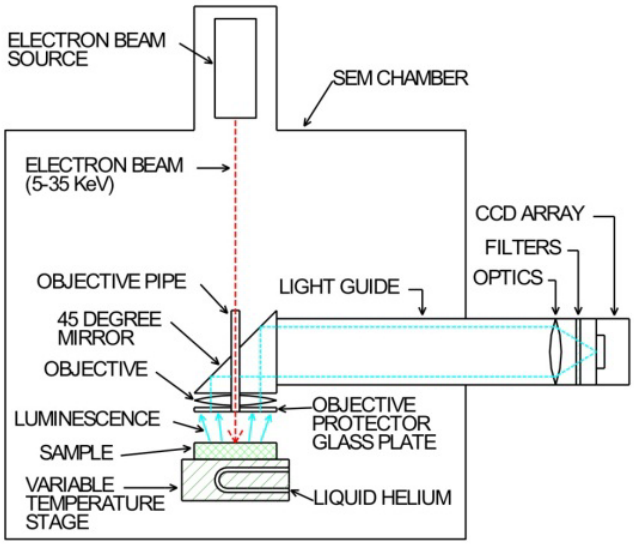

Figure 6. JEOL 840A experimental setup for transport imaging. From [4]

This retractable arm is equipped with a small objective pipe which allows the electron beam to reach the sample surface while the microscope objective lens is in place. The retractable arm is also equipped with an angled mirror which reflects recombination luminescence back to the attached CCD array camera at a magnification of 20×. The CCD array camera is composed of a thermoelectrically-cooled, 1284 × 1472 array of Silicon pixels, with each pixel measuring $6.8\mu m^2$. The combined spatial resolution of the optical microscope and CCD array camera is $0.4\mu m$/pixel, which allows for high-resolution imaging of the sample surface at the μm order of magnitude. The Silicon CCD detects EHP recombination luminescence in the 300–900 nm wavelength range, allowing the study of semiconductors with bandgaps ranging from 1.38 eV to 4.13 eV respectively.

The sample stage of the JEOL 840A SEM can be maintained at room temperature (295K) or lowered to liquid helium (5K) or liquid nitrogen (77K) temperatures. Lowering the sample temperature increases imaging resolution by decreasing the thermal generation of charge carriers, thereby increasing signal-to-noise ratio on the luminescence profile. This is accomplished by attaching a dewar filled with helium or nitrogen via a transfer line which supplies the cryogen to the SEM stage. To generate the desired electron interaction volume (Figure 4), electron beam excitation voltages can be

adjusted from 1.0 keV to 30.0 keV and probe currents can be adjusted from 1×10^{-11} A to 6×10^{-10} A. The SEM magnification can be adjusted from 20× to 10,000× to view a specific region of the sample, though focus becomes more difficult to maintain beyond 5,000×. Most transport imaging experiments for CZT are successfully conducted in the 10.0 keV range, with probe currents of 3×10^{-10} A and magnification settings of 1200×.

The JEOL 840A SEM can be operated in spot mode, line mode, or picture mode depending on the user's imaging preference. Spot mode focuses the electron beam at a point on the sample surface, which generates a surplus of EHPs at the impact point that diffuse symmetrically outward in a 360° pattern, creating a circularly-symmetric, luminescent diffusion pattern as the EHPs recombine (Figure 7). Line mode moves the electron beam back and forth quickly along an axis, forming an excess of EHPs that also diffuse in a 360° pattern, though they effectively diffuse orthogonally away from the axis and illuminate a linear pattern as they recombine. Picture mode rasters the electron beam back and forth quickly over a rectangular area of the sample, generating a surplus of EHPs over a region of interest that recombine, highlighting spatial variations of material properties.

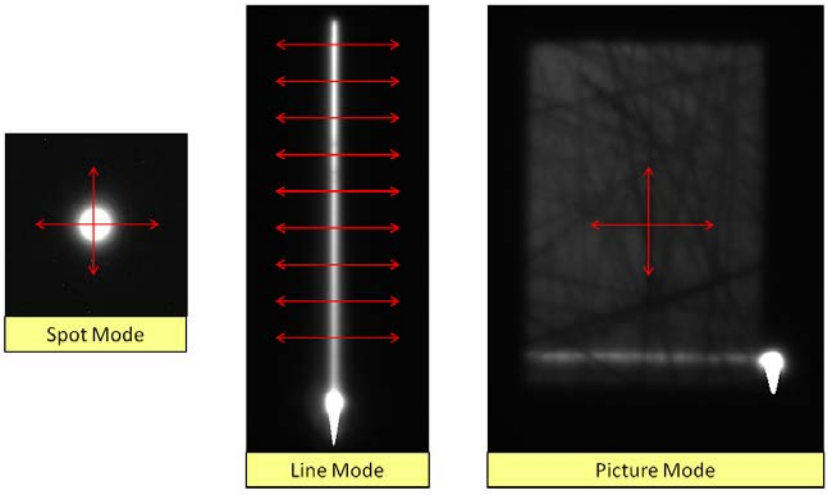

Figure 7. SEM imaging options: Spot, line, or picture mode

In transport imaging, picture mode is initially used at a magnification between 500× to 1500× to search for crystal defects appearing in the luminescent area. Once these defects are located, line scans are performed through the defect and compared with

line scans performed in the immediate vicinity. Two methods can be used for transport imaging: method 1 and method 2 (Figure 8). Method 1 utilizes a sequential series of line scans from left to right (A through I) in $2\mu m$ intervals encompassing the defect and the surrounding area. The region between 1 and 2 is specifically analyzed. Method 2 utilizes only one line scan through the defect, and more uniform regions between 1 and 2 are compared with regions 5 and 6 through the defect.

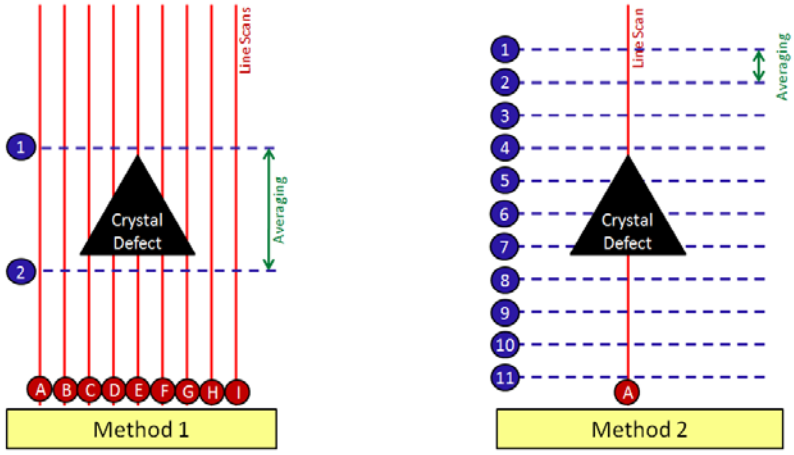

Figure 8. Methods of transport imaging performed to study the region around a crystal defect

C. MATHEMATICAL MODEL OVERVIEW

The luminescent recombination pattern of EHPs can be modeled as intensity I [counts] as a function of position r [m], where r is the radial distance $\left(r = \sqrt{x^2 + y^2 + z^2}\right)$ from the electron beam impact point, and (x,y,z) is the 3D position within the sample where luminescent recombination occurs. Both radial and Cartesian coordinates will be used to define the axes, origin, and position within the sample for the duration of this model development (Figure 9).

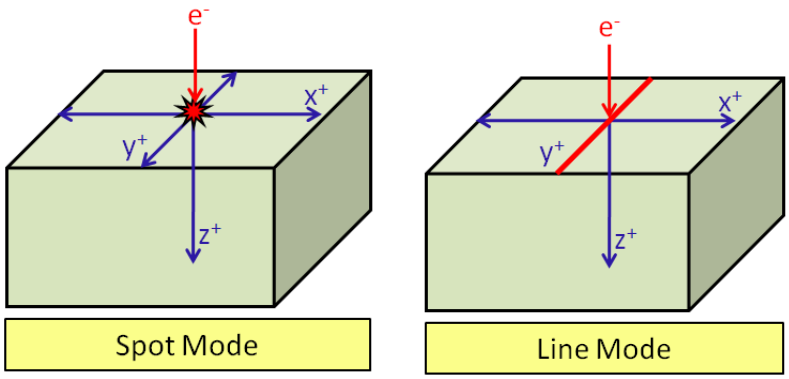

Figure 9. SEM operated in spot and line modes. After [4]. The electron beam impact point is represented in red, while the diffusion path of electrons and holes is represented in blue.

In spot mode excitation, the EHPs diffuse radially outward from the electron beam impact point, creating the circularly-symmetric illumination pattern on the surface depicted in Figure 7 which can be described mathematically by Equation (8) [4]. This is a three-dimensional (3D) model where L_d is the diffusion length [m].

$$I(r) \propto \left(\frac{1}{r}\right) e^{-\left(\frac{r}{L_d}\right)} \tag{8}$$

In line mode excitation, the EHPs diffuse from the electron beam impact axis, creating the linearly-symmetric illumination pattern also depicted in Figure 7. If the assumption is made that the electron beam moves back and forth so fast that intensity does not vary along the impact axis y, then intensity I only changes in the x and z directions and the 3D model reduces to 2D. Equation (9) reflects this 2D representation, where K_0 is a modified zeroth order Bessel function of the second kind.

$$I(r) \sim K_0\left(\frac{r}{L_d}\right) \tag{9}$$

Note that this modified Bessel function has a singularity at the origin, $K_0(0) \to \infty$ [4].

D. DETAILS OF THE MATHEMATICAL MODEL

To more accurately model the luminescent recombination pattern of EHPs as a function of position, however, it is helpful to determine the concentration of free charge

carriers at these positions within the material, and include the effect of the surface and the integration of photons emerging from various depths. After all, it is the presence of free charge carriers that permits recombination luminescence. A mathematical model has been developed by Blaine et. al. [8-9] to extract the diffusion length L_d and the mobility-lifetime product $\mu\tau$ from the luminescence distribution using the 2D model for transport imaging in bulk material. His model, which is described in detail over the next few pages, defines the following parameters:

$u(\vec{r})$ = Concentration of free charge carriers at position $\vec{r}$ within the sample

g = charge carrier generation rate per unit length [*charge/cm·s*].

D = Diffusivity of free charge carriers in the material [m^2/s]

S = Surface recombination velocity [*m/s*]

τ = Recombination lifetime [*s*]

z_0 = Electron beam penetration depth [*m*]

$V = S/D$ = surface recombination velocity divided by diffusivity [*1/m*]

L_d = Diffusion length [*m*]

The line mode of the SEM reduces the three-dimensional model into one of two dimensions by eliminating variation of charge carriers along the *y*-axis. As such, the free charge carrier vector $u(\vec{r})$ or $u(x, y, z)$ reduces to $u(x, z)$. More specifically, the SEM line mode generates an "infinite" line source of charge q with rate g per unit distance and as such, the charge carrier concentration in the *y*-axis is constant. The electron beam penetration depth z_0 is the center of mass (CoM) of the electron interaction volume depicted in Figure 10 that changes based on the SEM's electron beam acceleration voltage, and is usually within ~*1* μm of the surface.

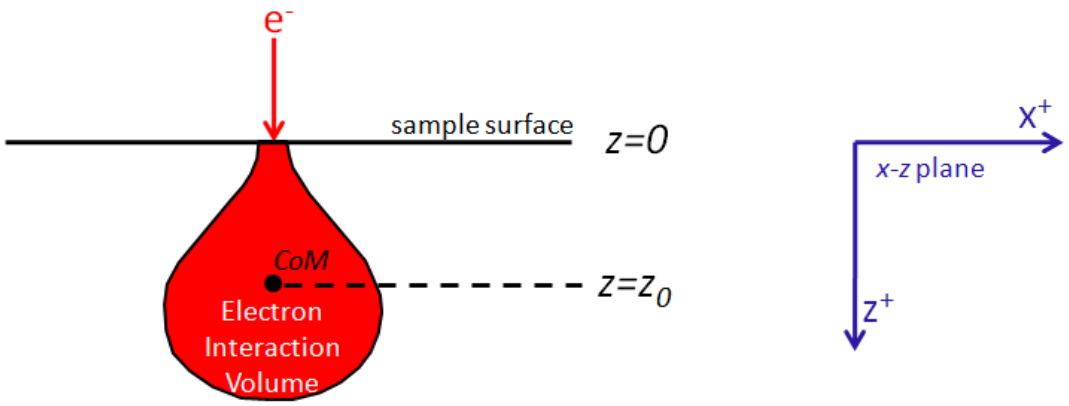

Figure 10. Model of electron beam penetration depth z_0

The diffusion of charge carriers away from this electron interaction volume CoM is described by the continuity equation (10). The time rate of change of the charge carrier concentration depends on the SEM beam's charge carrier generation rate, recombination rate, and carrier diffusion.

$$\frac{\partial}{\partial t}u\left(\vec{r},t\right)=G-R+\frac{1}{e}\left(\nabla\cdot\vec{J}\right) \tag{10}$$

The variable $u\left(\vec{r},t\right)$ is the charge carrier concentration at radial distance $\vec{r}$ away from the CoM at time t [s]. G is the charge carrier concentration generation rate [*carriers/s*], e is the elementary charge [C], R is the charge carrier concentration recombination rate [*carriers/s*], and $\vec{J}$ is the current density [A/m^2]. Since the SEM's line mode creates a constant concentration of free charge carriers along the y-axis at any time t, there is no rate of change, and thus, a steady state condition is reached. The LHS of Equation (10) can now be set to zero.

$$\frac{\partial}{\partial t}u\left(\vec{r},t\right)=0\,. \tag{11}$$

The 2D Dirac delta function models the electron interaction volume CoM as a point source that supplies free charge carriers at the point z_0 beneath the sample surface. At the point $\left(x,z\right)=\left(0,z_0\right)$, the generation rate G of Equation (10) becomes

$$G=g\cdot\delta(x)\delta(z-z_0) \tag{12}$$

At steady state, the charge carrier recombination rate R of Equation (10) becomes

$$R = \frac{u(\vec{r})}{\tau} \quad \text{or} \quad R = \frac{u(x,z)}{\tau} \tag{13}$$

In its contact-free application, transport imaging determines minority carrier diffusion in the absence of an electric field ($E = 0$). As such, the current density equation $\vec{J} = e\mu NE + eD\nabla u(\vec{r})$ reduces to

$$\vec{J} = eD\nabla u(\vec{r}) \tag{14}$$

Equations (11)–(14) can now be substituted into Equation (10) to arrive at the minority carrier diffusion equation, which models the diffusion of free charge carriers in the sample's x-z plane.

$$D\nabla^2 u(x,z) - \frac{1}{\tau}u(x,z) + g \cdot \delta(x)\delta(z - z_0) = 0 \tag{15}$$

Recall Equation (5) for diffusion length $L_d = \sqrt{D\tau}$. Rearranging this formula and substituting it into Equation (15) reveals the modified minority carrier diffusion equation (16) as follows

$$\nabla^2 u(x,z) - \frac{1}{L^2}u(x,z) + \frac{g}{D} \cdot \delta(x)\delta(z - z_0) = 0 \tag{16}$$

In order to complete the model, boundary conditions must be specified. This is done by assuming that the free charge carrier concentration $u(\vec{r})$ goes to zero infinitely far away from the source. In other words, $u(\vec{r}) \to 0$ as $\vec{r} \to \infty$. In Cartesian coordinates, $u(x,z) \to 0$ as $\sqrt{x^2 + y^2} \to \infty$.

The surface boundary condition is then determined by assuming that the diffusion of charge normal to the surface is proportional to the intensity of the charge normal to the surface, with proportionality constant S. Recalling that the vector normal to the sample surface is $\hat{z}$, the flux of carrier concentration in the $+\hat{z}$ direction is then defined as $D\frac{\partial}{\partial z}u(x,z)$ so that

$$D\frac{\partial u}{\partial z}(x,z) = S(x,z) \text{ at the boundary } z = 0 \tag{17}$$

A new material parameter V [*1/m*] can now be defined as surface recombination velocity [*m/s*] divided by the free charge carrier diffusivity constant [m^2/s]. Equation (17) can therefore be rewritten as:

$$\frac{\partial u}{\partial z}(x,z) = Vu(x,z) \tag{18}$$

The solution to the modified minority carrier diffusion equation (16) is the free-space Green's function $u_{FS}(r)$, solved using cylindrical symmetry and standard Green's function methods, where K_0 is the modified Bessel function of the second kind and $r = \sqrt{x^2 + (z - z_0)^2}$, since the point source for the model resides at the point $(x,z) = (0,z_0)$.

$$u_{FS}(r) = \frac{g}{2\pi D} K_0\left(\frac{r}{L}\right) \tag{19}$$

The Fourier transform $F(\omega) = \int_{-\infty}^{\infty} f(x,z)e^{i\omega x}dx$ can also be used to solve the modified minority carrier diffusion equation (16), resulting in the following:

$$0 = \int_{-\infty}^{\infty}\left[\nabla^2 u(x,z) - \frac{1}{L^2}u(x,z) + \frac{g}{D}\cdot\delta(x)\delta(z-z_0)\right]e^{-i\omega x}dx \tag{20}$$

This yields the following result

$$0 = -\omega^2 U(\omega,z) + \frac{\partial^2 U}{\partial z^2}(\omega,z) - \frac{1}{L^2}U(\omega,z) + \frac{g}{D}\cdot\delta(z-z_0) \tag{21}$$

Equation (22) is a second-order, non-homogeneous differential equation, and its solution is:

$$U(\omega,z) = \frac{g}{2\alpha D}e^{-\alpha|z-z_0|} \tag{22}$$

$$\text{where } \alpha = \sqrt{\omega^2 + \frac{1}{L_d^{\,2}}} \tag{23}$$

The inverse Fourier transform $f(x,z)=\frac{1}{2\pi}\int_{-\infty}^{\infty}F(\omega,z)e^{-i\omega x}d\omega$ can now be used to return Equation (22) to the *x*-domain.

$$u(x,z)=\frac{1}{2\pi}\int_{-\infty}^{\infty}\left[\frac{g}{2\alpha D}e^{-\alpha|z-z_0|}\right]e^{-i\omega x}d\omega \tag{24}$$

Equation (24) can be simplified into the following form

$$u(x,z)=\frac{g}{2\pi D}\int_{-\infty}^{\infty}\frac{1}{2\alpha}e^{-i\omega x-\alpha|z-z_0|}d\omega \tag{25}$$

A comparison of Equations (19) and Equation (25) yields the following relationship for the modified Bessel function K_0.

$$K_0\left(\frac{r}{L}\right)=\int_{-\infty}^{\infty}\frac{1}{2\alpha}e^{-i\omega x-\alpha|z-z_0|}d\omega \tag{26}$$

Yet another solution to differential equation (21) is given by:

$$U(\omega,z)=\begin{cases}Be^{\alpha z}+Ce^{-\alpha z} & \text{for } 0\le z<z_0\\ Ae^{-\alpha z} & \text{for } z>z_0\end{cases} \tag{27}$$

Applying the surface boundary condition in Equation (18) yields the following result:

$$\alpha\left(B-C\right)=V\left(B+C\right) \tag{28}$$

Both portions of the piecewise-defined Equation (28) must equal each other at the boundary $z=z_0$. Setting both piece-wise portions equal to each other yields the following equation.

$$Be^{\alpha z_0}+Ce^{-\alpha z_0}=Ae^{-\alpha z_0} \tag{29}$$

Equation (29) can be rearranged into the following form

$$Be^{\alpha z_0}+Ce^{-\alpha z_0}-Ae^{-\alpha z_0}=0 \tag{30}$$

The derivatives of both piece-wise portions of Equation (27) must satisfy the following jump condition:

$$\left.\frac{dU}{dz}\right|_{z_0-}^{z_0+} = -\frac{g}{D} \tag{31}$$

Applying this jump condition to Equation (30) yields the following result:

$$-\alpha A e^{-\alpha z_0} - \alpha B e^{\alpha z_0} + \alpha C e^{-\alpha z_0} = -\frac{g}{D} \tag{32}$$

Substituting Equation (29) into Equation (32) and solving for B yields the following:

$$B = \frac{g}{2\alpha D} e^{-\alpha z_0} \tag{33}$$

Substituting Equation (33) into Equation (29) and solving for C yields the following:

$$C = \frac{g}{2\alpha D}\left(\frac{\alpha - V}{\alpha + V}\right) e^{-\alpha z_0} \tag{34}$$

Substituting Equation (33) and Equation (34) into Equation (30) and solving for A yields the following:

$$A = \frac{g}{2\alpha D} e^{\alpha z_0} + \frac{g}{2\alpha D}\left(\frac{\alpha - V}{\alpha + V}\right) e^{-\alpha z_0} \tag{35}$$

Equations (33), (34), and (35) for coefficients B, C, and A respectively can now be substituted back into Equation (28) to yield the following piece-wise defined function:

$$U(\omega, z) = \begin{cases} \left[\frac{g}{2\alpha D} e^{-\alpha z_0}\right] e^{\alpha z} + \left[\frac{g}{2\alpha D}\left(\frac{\alpha - V}{\alpha + V}\right) e^{-\alpha z_0}\right] e^{-\alpha z} & \text{for } 0 \le z \le z_0 \\ \left[\frac{g}{2\alpha D} e^{\alpha z_0} + \frac{g}{2\alpha D}\left(\frac{\alpha - V}{\alpha + V}\right) e^{-\alpha z_0}\right] e^{-\alpha z} & \text{for } z \ge z_0 \end{cases} \tag{36}$$

Equation (36) can be simplified into the following form

$$U(\omega, z) = \frac{g}{2\alpha D} \begin{cases} e^{\alpha(z - z_0)} + \left(\frac{\alpha - V}{\alpha + V}\right) e^{-\alpha(z + z_0)} & \text{for } 0 \le z \le z_0 \\ e^{-\alpha(z - z_0)} + \left(\frac{\alpha - V}{\alpha + V}\right) e^{-\alpha(z + z_0)} & \text{for } z \ge z_0 \end{cases} \tag{37}$$

The inverse Fourier transform $f(x,z)=\frac{1}{2\pi}\int_{-\infty}^{\infty}F(\omega,z)e^{-i\omega x}d\omega$ can now be used to return Equation (37) back to the *z* domain.

$$u(x,z)=\frac{g}{2\pi D}\begin{cases}\int_{-\infty}^{\infty}\frac{1}{2\alpha}\left[e^{\alpha(z-z_0)}+\left(\frac{\alpha-V}{\alpha+V}\right)e^{-\alpha(z+z_0)}\right]e^{-i\omega x}d\omega & \text{for } 0\le z\le z_0\\ \int_{-\infty}^{\infty}\frac{1}{2\alpha}\left[e^{-\alpha(z-z_0)}+\left(\frac{\alpha-V}{\alpha+V}\right)e^{-\alpha(z+z_0)}\right]e^{-i\omega x}d\omega & \text{for } z\ge z_0\end{cases} \tag{38}$$

We now separate the equation $\left(\frac{\alpha-V}{\alpha+V}\right)$ into two parts using partial fractions:

$$\left(\frac{\alpha-V}{\alpha+V}\right) = \frac{\alpha+V-2V}{\alpha+V} = \frac{\alpha+V}{\alpha+V}-\frac{2V}{\alpha+V} = 1-\frac{2V}{\alpha+V} \tag{39}$$

This allows us to separate Equation (38) into three parts

$$\begin{aligned}u(x,z)=&\frac{g}{2\pi D}\int_{-\infty}^{\infty}\frac{1}{2\alpha}e^{-\alpha|z-z_0|-i\omega x}d\omega\\ &+\frac{g}{2\pi D}\int_{-\infty}^{\infty}\frac{1}{2\alpha}e^{-\alpha(z+z_0)-i\omega x}d\omega\\ &-2V\frac{g}{2\pi D}\int_{-\infty}^{\infty}\left(\frac{1}{2\alpha(\alpha+V)}\right)e^{-\alpha(z+z_0)-i\omega x}d\omega\end{aligned} \tag{40}$$

The intent now is to shape all three portions of Equation (40) into a form that matches the right side of Equation (27). To accomplish this, the integrand of the third portion of Equation (40) must be rewritten as follows:

$$\begin{aligned}\left(\frac{1}{2\alpha(\alpha+V)}\right)e^{-\alpha(z+z_0)-i\omega x}&=\frac{1}{2\alpha}\left[\frac{1}{\alpha+V}e^{-\alpha(z+z_0)}\right]e^{-i\omega x}\\ &=\frac{1}{2\alpha}\left[e^{z_0V}\int_{z_0}^{\infty}e^{-\alpha z}e^{-(\alpha+V)\zeta}d\zeta\right]e^{-i\omega x}\end{aligned} \tag{41}$$

Equation (41) is now substituted into Equation (40) to form the following equation:

$$u(x,z)=\frac{g}{2\pi D}\int_{-\infty}^{\infty}\frac{1}{2\alpha}e^{-\alpha|z-z_0|-i\omega x}d\omega$$
$$+\frac{g}{2\pi D}\int_{-\infty}^{\infty}\frac{1}{2\alpha}e^{-\alpha(z+z_0)-i\omega x}d\omega \tag{42}$$
$$-2V\frac{g}{2\pi D}\int_{-\infty}^{\infty}\frac{1}{2\alpha}\left[e^{z_0V}\int_{z_0}^{\infty}e^{-\alpha z}e^{-(\alpha+V)\zeta}d\zeta\right]e^{-i\omega x}d\omega$$

The order of integration of the third term can be reversed as follows:

$$u(x,z)=\frac{g}{2\pi D}\int_{-\infty}^{\infty}\frac{1}{2\alpha}e^{-\alpha|z-z_0|-i\omega x}d\omega$$
$$+\frac{g}{2\pi D}\int_{-\infty}^{\infty}\frac{1}{2\alpha}e^{-\alpha(z+z_0)-i\omega x}d\omega \tag{43}$$
$$-\frac{gV}{\pi D}e^{z_0V}\int_{z_0}^{\infty}e^{-V\zeta}\left[\int_{-\infty}^{\infty}\frac{1}{2\alpha}e^{-\alpha(z+\zeta)-i\omega x}d\omega\right]d\zeta$$

Now that all three portions of Equation (43) match the form of the right side of Equation (27), it can be rewritten as a series of three modified Bessel functions of the second kind, recalling that $r=\sqrt{x^2+\left(z-z_0\right)^2}$ for the origin at the point $\left(x,z\right)=\left(0,z_0\right)$.

$$u(x,z)=\frac{g}{2\pi D}K_0\left(\frac{\sqrt{x^2+\left(z-z_0\right)^2}}{L}\right)$$
$$+\frac{g}{2\pi D}K_0\left(\frac{\sqrt{x^2+\left(z+z_0\right)^2}}{L}\right) \tag{44}$$
$$-\frac{gV}{\pi D}e^{z_0V}\int_{z_0}^{\infty}e^{-V\zeta}K_0\left(\frac{\sqrt{x^2+\left(z+\zeta\right)^2}}{L}\right)d\zeta$$

For ease of integration, Equation (44) will now be split into three components such that $u(x,z)=u_1(x,z)+u_2(x,z)+u_3(x,z)$.

$$u_1(x,z)=\frac{g}{2\pi D}K_0\left(\frac{\sqrt{x^2+\left(z-z_0\right)^2}}{L}\right) \tag{45}$$

$$u_2(x,z) = \frac{g}{2\pi D} K_0\left(\frac{\sqrt{x^2 + (z+z_0)^2}}{L}\right) \tag{46}$$

$$u_3(x,z) = -\frac{gV}{\pi D} e^{z_0 V} \int_{z_0}^{\infty} e^{-V\zeta} K_0\left(\frac{\sqrt{x^2 + (z+\zeta)^2}}{L}\right) d\zeta \tag{47}$$

Equations (45)-(47) will now be integrated with respect to *z* to arrive at a function $u(x)$ which will model free charge carrier concentration integrated through the sample, which is the purpose of the math model. The limits of integration will be from $z = 0$ to $z = \infty$.

Equation (47) will be integrated first, since it is the most complex. Equation (47) is integrated with respect to z as follows:

$$u_3(x) = -\frac{gV}{\pi D} e^{z_0 V} \int_0^{\infty} \int_{z_0}^{\infty} e^{-V\zeta} K_0\left(\frac{\sqrt{x^2 + (z+\zeta)^2}}{L}\right) d\zeta dz \tag{48}$$

The following *u*-substitution method is then performed on Equation (48), yielding the intermediate result in Equation (49).

$$\boxed{\text{let } \tau = z + \zeta \text{ and let } d\tau = \text{dz}}$$

$$u_3(x) = -\frac{gV}{\pi D} e^{z_0 V} \int_0^{\infty} e^{zV} \int_{z+z_0}^{\infty} e^{-V\tau} K_0\left(\frac{\sqrt{x^2 + \tau^2}}{L}\right) d\tau dz \tag{49}$$

Integration by parts is then performed on Equation (49) as follows:

$$\boxed{\begin{array}{l} \text{let } w = \displaystyle\int_{z+z_0}^{\infty} e^{-v\tau} K_0\left(\frac{\sqrt{x^2+\tau^2}}{L}\right) d\tau \quad \text{and} \quad \text{let } dv = e^{Vz} dz; \\ \text{let } dw = -e^{-v(z+z_0)} K_0\left(\frac{\sqrt{x^2+(z+z_0)^2}}{L}\right) dz \quad \text{and} \quad \text{let } v = \frac{1}{V} e^{Vz}; \end{array}}$$

Then,

$$u_3(x) = \frac{g}{\pi D} e^{z_0 V} \int_{z_0}^{\infty} e^{-V\tau} K_0\left(\frac{\sqrt{x^2+\tau^2}}{L}\right) d\tau - \frac{g}{\pi D} \int_0^{\infty} K_0\left(\frac{\sqrt{x^2+\left(z+z_0\right)^2}}{L}\right) dz \qquad (50)$$

For further ease of integration, Equation (50) will now be split into two components such that $u_3(x) = u_{3a}(x) + u_{3b}(x)$.

$$u_{3a}(x) = \frac{g}{\pi D} e^{z_0 V} \int_{z_0}^{\infty} e^{-V\tau} K_0\left(\frac{\sqrt{x^2+\tau^2}}{L}\right) d\tau \qquad (51)$$

$$u_{3b}(x) = -\frac{g}{\pi D} \int_0^{\infty} K_0\left(\frac{\sqrt{x^2+\left(z+z_0\right)^2}}{L}\right) dz \qquad (52)$$

Before proceeding further, note that Equation (46) and Equation (52) can be combined. This will occur once all *u*-substitution efforts are complete.

The following *u*-substitution method is now performed on Equation (51) as follows:

let $\xi = \frac{\sqrt{x^2+\tau^2}}{L}$ and $\tau = L\sqrt{\xi^2 - \left(x/L\right)^2}$;

let $d\xi = \frac{\sqrt{\xi^2+\left(x/L\right)^2}}{L\xi} d\tau$ and $d\tau = \frac{L\xi}{\sqrt{\xi^2+\left(x/L\right)^2}} d\xi$;

Then we get:

$$u_{3a}(x) = 2L \int_{\frac{\sqrt{x^2+z_0^2}}{L}}^{\infty} e^{V\left(z_0 - L\sqrt{\xi^2-\left(x/L\right)^2}\right)} K_0(\xi) \left(\frac{\xi}{\sqrt{\xi^2-\left(x/L\right)^2}}\right) d\xi \qquad (53)$$

Equation (45) is integrated with respect to z as follows:

$$u_1(x) = \frac{g}{2\pi D} \int_0^{\infty} K_0\left(\frac{\sqrt{x^2+\left(z-z_0\right)^2}}{L}\right) dz \qquad (54)$$

The *u*-substitution method is then performed on Equation (54) by writing:

$$\text{let } \xi = \frac{\sqrt{x^2 + (z - z_0)^2}}{L} \text{ and } z - z_0 = \pm L\sqrt{\xi^2 - \left(x/L\right)^2};$$

$$\text{let } d\xi = \frac{\sqrt{\xi^2 - \left(x/L\right)^2}}{L\xi} dz \text{ and } dz = \frac{L\xi}{\sqrt{\xi^2 - \left(x/L\right)^2}} d\xi;$$

We get:

$$u_1(x) = \frac{gL}{\pi D} \int_{\frac{x}{L}}^{\frac{\sqrt{x^2+z_0^2}}{L}} K_0(\xi) \left(\frac{\xi}{\sqrt{\xi^2 - \left(x/L\right)^2}} \right) d\xi + \frac{gL}{2\pi D} \int_{\frac{\sqrt{x^2+z_0^2}}{L}}^{\infty} K_0(\xi) \left(\frac{\xi}{\sqrt{\xi^2 - \left(x/L\right)^2}} \right) d\xi \quad (55)$$

Equation (46) is added to Equation (52) and integrated with respect to z as follows:

$$u_2(x) = -\frac{g}{2\pi D} \int_0^{\infty} K_0 \left(\frac{\sqrt{x^2 + (z + z_0)^2}}{L} \right) dz \quad (56)$$

The *u*-substitution method is then performed on Equation (56), yielding the following:

$$\text{let } \xi = \frac{\sqrt{x^2 + (z + z_0)^2}}{L} \text{ and } z + z_0 = \pm L\sqrt{\xi^2 - \left(x/L\right)^2};$$

$$\text{let } d\xi = \frac{\sqrt{\xi^2 - \left(x/L\right)^2}}{L\xi} dz \text{ and } dz = \frac{L\xi}{\sqrt{\xi^2 - \left(x/L\right)^2}} d\xi;$$

We arrive at:

$$u_2(x) = -\frac{gL}{\pi D} \int_{\frac{\sqrt{x^2+z_0^2}}{L}}^{\infty} K_0(\xi) \left(\frac{\xi}{\sqrt{\xi^2 - \left(x/L\right)^2}} \right) d\xi \quad (57)$$

Equations (53), (55), and (57) are now combined to get:

$$u(x)=\frac{gL}{\pi D}\int_{\frac{x}{L}}^{\frac{\sqrt{x^2+z_0^2}}{L}} K_0(\xi)\left(\frac{\xi}{\sqrt{\xi^2-\left(x/L\right)^2}}\right)d\xi + \frac{gL}{\pi D}\int_{\frac{\sqrt{x^2+z_0^2}}{L}}^{\infty} e^{V\left(z_0-L\sqrt{\xi^2-\left(x/L\right)^2}\right)} K_0(\xi)\left(\frac{\xi}{\sqrt{\xi^2-\left(x/L\right)^2}}\right)d\xi \tag{58}$$

Perform *u*-substitution one final time:

$$\text{let } v=-z_0+L\sqrt{\xi^2-\left(x/L\right)^2} \text{ and } \xi=\frac{\sqrt{\left(u+z_0\right)^2+x^2}}{L};$$

$$\text{let } dv=\frac{L\xi}{\sqrt{\xi^2-\left(x/L\right)^2}}d\xi \text{ and } d\xi=\frac{\sqrt{\xi^2-\left(x/L\right)^2}}{L\xi}du$$

Finally, we arrive at:

$$u(x)=\frac{g}{\pi D}\left[\int_{-z_0}^{0} K_0\left(\frac{\sqrt{\left(u+z_0\right)^2+x^2}}{L}\right)du \quad + \quad \int_{0}^{\infty} e^{-Vu}K_0\left(\frac{\sqrt{\left(u+z_0\right)^2+x^2}}{L}\right)du\right] \tag{59}$$

A new material parameter B [*carriers/m*^{3}] can now be defined as the carrier generation rate *g* [*carriers/m*s*] divided by π times the carrier diffusion constant *D* [m^2/s]. This parameter B, defined in Equation 60, is called the carrier concentration prefactor.

$$\text{Let } B=\frac{g}{\pi D} \tag{60}$$

Carrier concentration at any position *x* on the sample surface can therefore be modeled as the sum of the two integrals:

$$u_{\text{model}}(x)=B\left[\int_{-z_0}^{0} K_0\left(\frac{\sqrt{\left(u+z_0\right)^2+x^2}}{L}\right)du \quad + \quad \int_{0}^{\infty} e^{-Vu}K_0\left(\frac{\sqrt{\left(u+z_0\right)^2+x^2}}{L}\right)du\right] \tag{61}$$

Limit analysis can now be performed on the final solution (61) to model behavior of charge carriers on the sample surface under different conditions. Since bulk

semiconductors are often unpassivated, free charge carriers generated within the sample can either recombine at the surface without radiating or they can be reflected back into the sample to recombine later [8]. If all carriers arriving at the surface recombine without radiating, then surface recombination velocity must be infinitely large ($S \to \infty$). Since $V=S/D$, this causes $V \to \infty$ and the second integral of Equation (61) reduces to zero. This is known as the Dirichlet boundary condition, and Equation (61) simplifies to:

$$u_{Dirichlet}(x) = B \int_{-z_0}^{0} K_0 \left(\frac{\sqrt{(u+z_0)^2 + x^2}}{L} \right) du \tag{62}$$

If, however, all carriers arriving at the surface are reflected back into the sample to recombine later, then surface recombination velocity must approach zero ($S \to 0$). This causes $V \to 0$ and the exponential term disappears from the second integral, causing the two integrals to combine into the following form, known as the Neumann boundary condition, and Equation (61) simplifies to:

$$u_{Neumann}(x) = B \int_{-z_0}^{\infty} K_0 \left(\frac{\sqrt{(u+z_0)^2 + x^2}}{L} \right) du \tag{63}$$

The correct model for a real detector material with an unpassivated surface often lies somewhere between the Dirichlet and Neumann cases. As such, Equation (61) can be thought of as the Dirichlet solution plus a correction term associated with a finite surface recombination rate.

$$u_{\text{model}}(x) = B \left[\int_{-z_0}^{0} K_0 \left(\frac{\sqrt{(u+z_0)^2 + x^2}}{L} \right) du + \int_{0}^{\infty} e^{-Vu} K_0 \left(\frac{\sqrt{(u+z_0)^2 + x^2}}{L} \right) du \right] \tag{64}$$

Dirichlet solution + correction term $I(V)$

E. ASYMPTOTIC EXPANSION OF THE CORRECTION TERM

Numerical integration of the correction term *I(V)* can become computationally expensive, time-consuming, and vulnerable to inaccuracy because of the infinite limit of integration. As such, it makes sense to simplify the correction term as much as possible

without losing accuracy. This can be done through a Taylor expansion of the modified Bessel function in the following manner when V is large. First, the correction term $I(V)$ must be formally defined as:

$$I(V) = \int_0^\infty e^{-Vu} K_0\left(\frac{\sqrt{(u+z_0)^2 + x^2}}{L}\right) du \tag{65}$$

Now, let

$$f(u) = K_0\left(\frac{\sqrt{(u+z_0)^2 + x^2}}{L}\right) \tag{66}$$

so that the correction term becomes:

$$I(V) = \int_0^\infty e^{-Vu} f(u) du \tag{67}$$

The Taylor expansion of $f(u)$ about $u = 0$ is:

$$f(u) = \frac{f(0)u^0}{0!} + \frac{f'(0)u^1}{1!} + \frac{f''(0)u^2}{2!} + \frac{f'''(0)u^3}{3!} + \ldots + \frac{f^n(0)u^n}{n!} \tag{68}$$

and the correction term becomes:

$$I(V) = \int_0^\infty e^{-Vu}\left(\frac{f(0)u^0}{0!} + \frac{f'(0)u^1}{1!} + \frac{f''(0)u^2}{2!} + \frac{f'''(0)u^3}{3!} + \ldots + \frac{f^n(0)u^n}{n!}\right) du \tag{69}$$

Integration of each term reveals the following formula for $I(V)$:

$$I(V) = \frac{f(0)}{V} + \frac{f'(0)}{V^2} + \frac{f''(0)}{V^3} + \frac{f'''(0)}{V^4} + \ldots + \frac{f^{(n)}(0)}{V^{n+1}} \tag{70}$$

Thus, the asymptotic expansion of Equation (61) becomes

$$u_{\text{model}}(x) = B\left[\int_{-z_0}^0 K_0\left(\frac{\sqrt{(u+z_0)^2 + x^2}}{L}\right) du + \frac{f(0)}{V} + \frac{f'(0)}{V^2} + \frac{f''(0)}{V^3} + \ldots + \frac{f^{(n)}(0)}{V^{n+1}}\right] \tag{71}$$

Equation (69) illustrates how the correction terms may look for finitely-large values of V. As a check to the previous conclusion, Equation (70) does in fact disappear completely as $V \to \infty$. To increase accuracy, more correction terms can be added.

To validate this model, two test cases were conducted with common semiconductor values for L, V, and Z_o. The results of these tests (1 and 2) are depicted below in Figures 11–12.

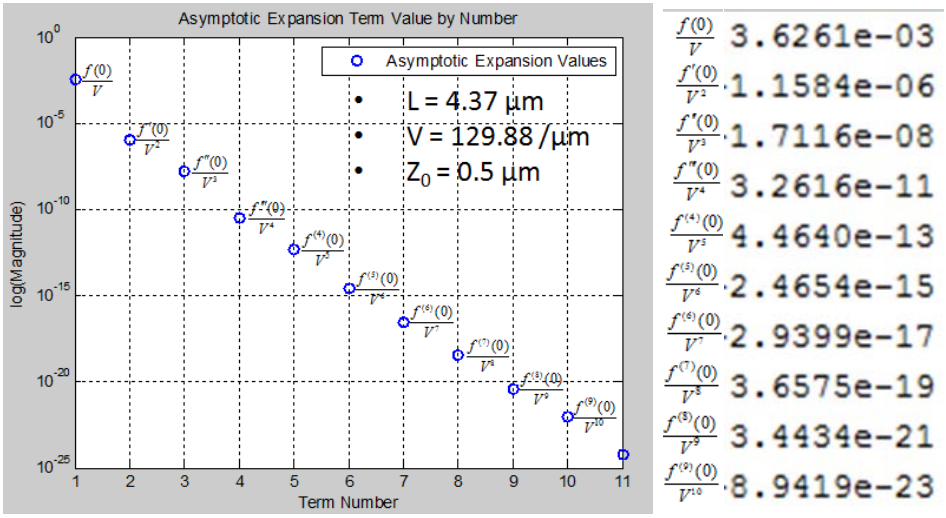

Figure 11. Correction term values from Test 1

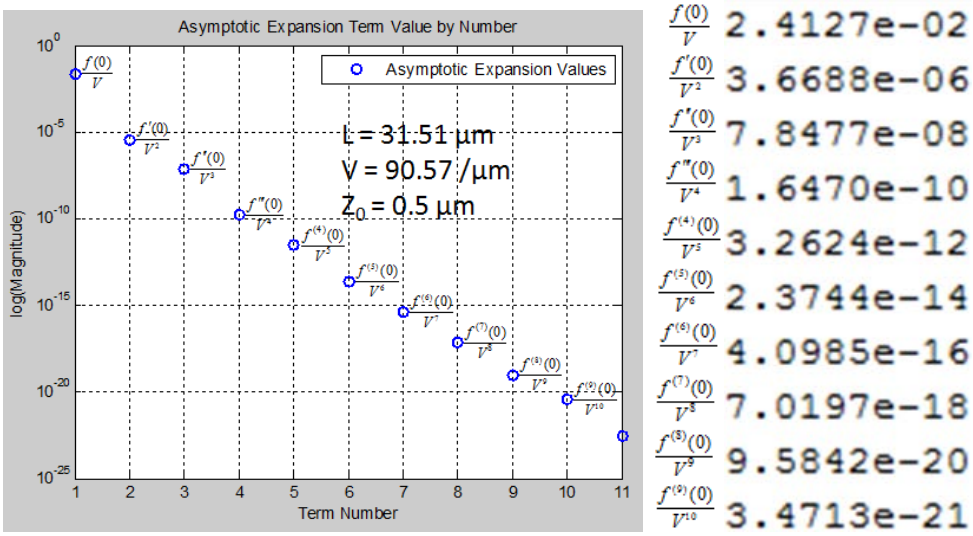

Figure 12. Correction term values from Test 2

These tests reveal that although accuracy does indeed improve as more correction terms are added, successive correction terms decrease by roughly three orders of

magnitude. Consequently, it makes sense to only include the first few correction terms. Thus, the three-correction-term asymptotic expansion of Equation (64) becomes:

$$u_{\text{model}}(x) = B\left[\int_{-z_0}^{0} K_0\left(\frac{\sqrt{(u+z_0)^2+x^2}}{L}\right)du + \frac{f(0)}{V} + \frac{f'(0)}{V^2} + \frac{f''(0)}{V^3}\right] \tag{72}$$

Dirichlet solution + correction term $I(V)$

F. NON-LINEAR LEAST SQUARES FITTING ALGORITHM

To successfully extract a sample's diffusion length L_d and mobility-lifetime product ($\mu\tau$) from a line scan image captured by the CCD array camera, the image must be fit to the mathematical model by means of a non-linear least squares fit algorithm. Previous transport imaging studies performed by Blaine et. al. employ the Levenberg-Marquardt least squares iterative method, which minimizes the function using a combination of Gauss-Newton methods and the method of steepest descent [8-9]. In this method, the user makes an initial guess of the sample's diffusion length L_d, surface recombination velocity/diffusivity constant V, and electron beam penetration depth Z_0. The algorithm then iterates, adjusting the model parameters to fit the diffusion pattern recorded in the CCD image until the convergence criterion is reached. Once the convergence criterion has been met, the algorithm yields the sample's L_d, V, and Z_0 values.

This thesis employs Newton's method as an independent least squares iterative algorithm to validate and extend the previous transport imaging analysis by Blaine et al. [8]. The algorithm for Newton's method is described as follows, with the mathematical model represented as:

$$u_{\text{model}}(B, L, V, Z_0, x) \tag{73}$$

The data captured from the CCD array camera is converted from a .jpg or .tif format to a vector of intensity I [*arbitrary units*] vs. position x [m] and is represented as:

$$u_{data}(x) \tag{74}$$

The error vector defining the cumulative difference between the model and the data is defined as follows:

$$\vec{e} = \vec{u}_{\mathrm{model}} - \vec{u}_{data} \tag{75}$$

The sum of squared residuals is then defined as follows:

$$\phi = \frac{1}{2}\left\|\vec{e}\right\|^2 = \frac{1}{2}\left\|\vec{u}_{\mathrm{model}} - \vec{u}_{data}\right\|^2 = \frac{1}{2}\vec{e}^T\vec{e} \tag{76}$$

The local search method is then employed to find the minimum values of the u_{model} function via the gradient of Equation (76):

$$\nabla\phi = \frac{1}{2}\begin{bmatrix} \dfrac{\partial\phi}{\partial B} \\ \dfrac{\partial\phi}{\partial L} \\ \dfrac{\partial\phi}{\partial V} \\ \dfrac{\partial\phi}{\partial Z_0} \end{bmatrix} = \begin{bmatrix} \vec{e}^T\dfrac{\partial\vec{u}_{\mathrm{model}}}{\partial B} \\ \vec{e}^T\dfrac{\partial\vec{u}_{\mathrm{model}}}{\partial L} \\ \vec{e}^T\dfrac{\partial\vec{u}_{\mathrm{model}}}{\partial V} \\ \vec{e}^T\dfrac{\partial\vec{u}_{\mathrm{model}}}{\partial Z_0} \end{bmatrix} \tag{77}$$

The Hessian of Equation (76) is then defined as follows:

$$\nabla^2\phi = \begin{bmatrix} \left(\frac{\partial\vec{u}_{\mathrm{model}}}{\partial B}^T\frac{\partial\vec{u}_{\mathrm{model}}}{\partial B} + \vec{e}^T\frac{\partial^2\vec{u}_{\mathrm{model}}}{\partial B^2}\right) & \left(\frac{\partial\vec{u}_{\mathrm{model}}}{\partial L}^T\frac{\partial\vec{u}_{\mathrm{model}}}{\partial B} + \vec{e}^T\frac{\partial^2\vec{u}_{\mathrm{model}}}{\partial L\partial B}\right) & \left(\frac{\partial\vec{u}_{\mathrm{model}}}{\partial V}^T\frac{\partial\vec{u}_{\mathrm{model}}}{\partial B} + \vec{e}^T\frac{\partial^2\vec{u}_{\mathrm{model}}}{\partial V\partial B}\right) & \left(\frac{\partial\vec{u}_{\mathrm{model}}}{\partial Z_0}^T\frac{\partial\vec{u}_{\mathrm{model}}}{\partial B} + \vec{e}^T\frac{\partial^2\vec{u}_{\mathrm{model}}}{\partial Z_0\partial B}\right) \\ \textit{symmetric} & \left(\frac{\partial\vec{u}_{\mathrm{model}}}{\partial L}^T\frac{\partial\vec{u}_{\mathrm{model}}}{\partial L} + \vec{e}^T\frac{\partial^2\vec{u}_{\mathrm{model}}}{\partial L^2}\right) & \left(\frac{\partial\vec{u}_{\mathrm{model}}}{\partial V}^T\frac{\partial\vec{u}_{\mathrm{model}}}{\partial L} + \vec{e}^T\frac{\partial^2\vec{u}_{\mathrm{model}}}{\partial V\partial L}\right) & \left(\frac{\partial\vec{u}_{\mathrm{model}}}{\partial Z_0}^T\frac{\partial\vec{u}_{\mathrm{model}}}{\partial L} + \vec{e}^T\frac{\partial^2\vec{u}_{\mathrm{model}}}{\partial Z_0\partial L}\right) \\ \textit{symmetric} & \textit{symmetric} & \left(\frac{\partial\vec{u}_{\mathrm{model}}}{\partial V}^T\frac{\partial\vec{u}_{\mathrm{model}}}{\partial V} + \vec{e}^T\frac{\partial^2\vec{u}_{\mathrm{model}}}{\partial V^2}\right) & \left(\frac{\partial\vec{u}_{\mathrm{model}}}{\partial Z_0}^T\frac{\partial\vec{u}_{\mathrm{model}}}{\partial V} + \vec{e}^T\frac{\partial^2\vec{u}_{\mathrm{model}}}{\partial Z_0\partial V}\right) \\ \textit{symmetric} & \textit{symmetric} & \textit{symmetric} & \left(\frac{\partial\vec{u}_{\mathrm{model}}}{\partial Z_0}^T\frac{\partial\vec{u}_{\mathrm{model}}}{\partial Z_0} + \vec{e}^T\frac{\partial^2\vec{u}_{\mathrm{model}}}{\partial {Z_0}^2}\right) \end{bmatrix} \tag{78}$$

Equations (70), (71), (74), and (75) may now be arranged into the Newton's method iteration, Equation (76).

$$\nabla\phi(B_{n+1}, L_{n+1}, V_{n+1}, Z_{0n+1}) = \nabla\phi(B_n, L_n, V_n, Z_{0n}) + \nabla^2\phi(B_n, L_n, V_n, Z_{0n})\begin{bmatrix} B_{n+1} - B_n \\ L_{n+1} - L_n \\ V_{n+1} - V_n \\ Z_{0n+1} - Z_{0n} \end{bmatrix} \tag{79}$$

The intent of the Newton's method algorithm is to iterate until the sum of squared residuals is minimized. To reflect this intention, the LHS of Equation (79) can be set to zero. Equation (79) may now be rearranged into a general form that presents the

minimized values of the sample's B, L_d, V, and Z_0 values as follows, where α_n is the step size determined by the Armijo rule and d_n is the descent direction:

$$\begin{bmatrix} B_{n+1} \\ L_{n+1} \\ V_{n+1} \\ Z_{0n+1} \end{bmatrix} = \begin{bmatrix} B_n \\ L_n \\ V_n \\ Z_{0n} \end{bmatrix} + \alpha_n d_n \tag{80}$$

If $\nabla^2\phi$ is positive definite (all non-negative eigenvalues), then the descent direction is defined as:

$$d_n = -\left[\nabla^2\phi\right]^{-1}\nabla\phi \tag{81}$$

However, if $\nabla^2\phi$ is not positive definite (at least one negative eigenvalue), then the descent direction must be defined as:

$$d_n = -\left[\nabla^2\phi + k_n I\right]^{-1}\nabla\phi \tag{82}$$

Note that in this modified descent direction, a factor k_n is added to each of the diagonal elements of the Hessian matrix to make it positive definite. This factor k_n, which is multiplied by the identity matrix in Equation (82), is defined as a value slightly larger than zero or the absolute value of the smallest eigenvalue of the Hessian matrix.

$$k_n > 0 \text{ or } \left|\text{smallest eigenvalue of } \nabla^2\phi\right| \tag{83}$$

The Armijo rule, which determines the step size α_n in Equation (80) is defined as:

$$\phi(B_n, L_n, V_n, Z_{0n}) - \phi(B_n, L_n, V_n, Z_{0n} + \alpha_n d_n) \geq -\sigma\alpha_n \left[\nabla\phi(B_n, L_n, V_n, Z_{0n})\right]^T d_n \tag{84}$$

where

$$\left\|\nabla\phi(B_{n+1}, L_{n+1}, V_{n+1}, Z_{0n+1}) - \nabla\phi(B_n, L_n, V_n, Z_{0n})\right\| \leq L\left\|\phi(B_{n+1}, L_{n+1}, V_{n+1}, Z_{0n+1}) - \phi(B_n, L_n, V_n, Z_{0n})\right\| \tag{85}$$

and

$$\text{m} \in \square^+ \quad , \quad 0 \leq \sigma \leq \frac{1}{2} \quad , \quad 0 \leq \beta \leq 1, \quad s_k = \frac{-(\nabla\phi)^T d_k}{L\left\|d_k\right\|^2}, \tag{86}$$

Note that the L in Equation (85) is the Lipschitz condition. To employ Newton's method, the user must first initialize the least squares algorithm by making an initial guess of the sample's property values and specifying the convergence criterion ε. Below are examples of initial guesses and convergence criterion:

$$\text{Initial guess } \begin{bmatrix} B_0 \\ L_0 \\ V_0 \\ Z_0 \end{bmatrix} = \begin{bmatrix} 4 \\ 10 \\ 8 \\ 0.5 \end{bmatrix} \quad \text{Convergence criterion } \varepsilon = 0.5 \text{ x } 10^{-3} \tag{87}$$

The algorithm then executes according to the following scheme:

Step #1: Calculate $u_{\text{model}}(B_n, L_n, V_n, Z_{0n}, x)$ with the values in Equation (87) for the first iteration only.

Step #2: Calculate error $\vec{e} = \vec{u}_{\text{model}}(B_n, L_n, V_n, Z_n, x) - \vec{u}_{data}(x)$

Step #3: Calculate sum of squared residuals $\phi = \frac{1}{2}\vec{e}^T\vec{e}$

Step #4: Calculate the gradient $\nabla\phi$

Step #5: Evaluate the convergence constant $c = \|\nabla\phi\|$. If the convergence criterion has been met, i.e. if $\|\nabla\phi\| < \varepsilon$, then the algorithm is complete. If not, then the algorithm continues to step #6.

Step #6: Calculate the Hessian $\nabla^2\phi$ using Equation (81) or (82) accordingly.

Step #7: Evaluate the eigenvalues of the Hessian $\nabla^2\phi$. If all eigenvalues are non-negative ($\nabla^2\phi$ is positive definite), then the descent direction d_n follows Equation (81). If not, then the decent direction follows Equation (82).

Step #8: Calculate the inverse of the Hessian matrix $\nabla^2\phi$.

Step #9: Determine the step size α_n of the iteration that satisfies the Armijo rule in Equation (84).

Step #10: Evaluate $\begin{bmatrix} B_{n+1} \\ L_{n+1} \\ V_{n+1} \\ Z_{0n+1} \end{bmatrix} = \begin{bmatrix} B_n \\ L_n \\ V_n \\ Z_{0n} \end{bmatrix} + \alpha_n d_n$

Step #11: Return to step #2 and continue to iterate until the convergence criterion has been met.

First-order and second-order partial derivatives of Equation (76) are needed to fill the gradient matrix (77) and the Hessian matrix (78). Newton's method can be used with either the exact or the asymptotically-expanded first-order and second-order partial derivatives, provided enough correction terms are included. Since the asymptotically-expanded solution does not have the infinite integral, it performs more quickly. The exact first and second order partial derivatives for the gradient and Hessian matrices are depicted explicitly in Appendix A.

G. LEAST SQUARES FIT EXAMPLE

This section illustrates the least squares fitting process from start to finish. First, an image of a line scan is taken with the CCD array camera attached to the SEM. The image is then imported into MATLAB and converted into a data matrix of intensity [*counts*] vs. x-y position [*m*]. A plot of the imported data appears in Figure 13.

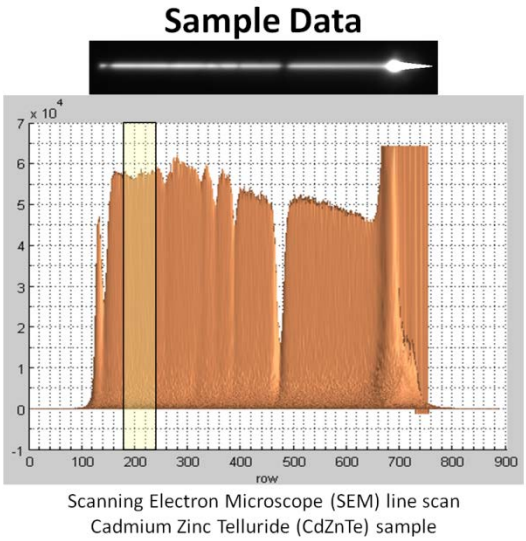

Figure 13. Plot of intensity as a function of position due to line scan excitation of a sample in the SEM

The user then selects the spatial region to be examined. In this example, the user has selected the 180–240 pixel range, highlighted in yellow. A 0.4 μm/pixel conversion means that this is a 24 μm region of interest. The region is averaged, normalized, and

plotted as a function of intensity [*counts*] vs. position x [μm] perpendicular to the line scan. The x-axis is converted from pixels to μm, and the 0-4 μm region of the x-axis is removed to avoid singularities at the origin for the two modified Bessel functions employed in Equation (61), which are fit to this data via the least squares algorithm.

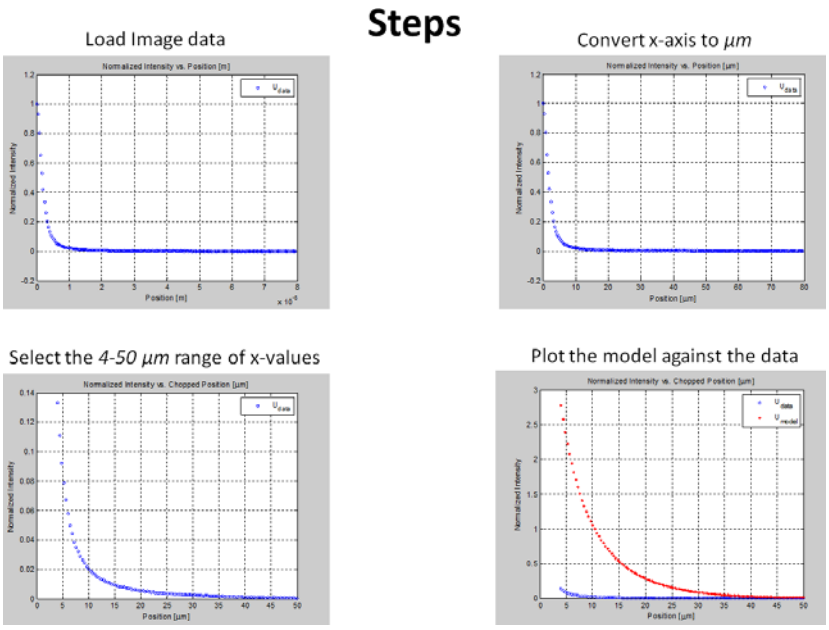

Figure 14. Least square fitting steps showing comparison between the data values (blue) and the mathematical model evaluated at the initial guess values B, L_d, V, and Z_0.

The vector of x-data (4-50μm in this example) is then passed to the least squares algorithm along with the user's initial guess for values of B, L_d, V, Z_0, and convergence criteria ε. The algorithm plots the results of the math model with the initial guess (red) next to the image data extracted from the CCD image (blue). Steps 1-11 are then executed repeatedly in a loop until convergence criteria is met. As the loop continues,the red model plot reduces to the blue image plot until the sum of squares residuals is minimized, the best fit is obtained, and both plots eventually overlap as depicted in Figure 15.

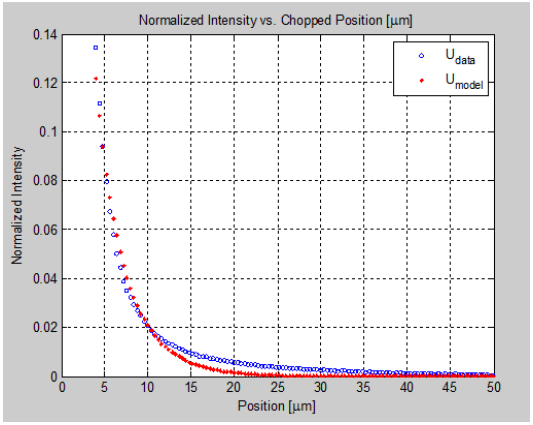

Figure 15. Least square fitting endstate

Once the convergence criterion has been met, the loop is broken and the least squares algorithm yields the values of B, L_d, V, and Z_0 for the sample. Equation (6) can then be used to convert diffusion length L_d to mobility-lifetime ($\mu\tau$) product if desired.

H. MODEL VALIDATION

To ensure that the mathematical model accurately reflects changes in diffusion length, a transport imaging scan of an intentionally damaged sample was analyzed. This sample was intentionally bombarded with protons in order to damage the crystal structure, decrease the lifetime, and ultimately reduce the semiconductor's diffusion length. Figure 16 depicts the CCD image of the SEM performing two spot mode scans on the sample surface. The left image is an image taken of an undamaged portion of the sample. The right image is an image taken of the radiation-damaged portion of the sample.

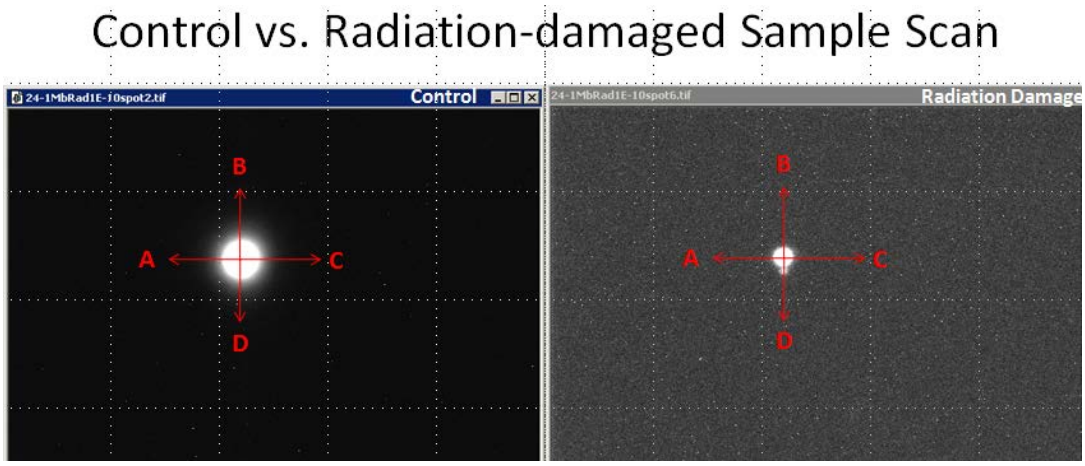

Figure 16. Luminescence images in control area vs. radiation-damaged area of sample

The diffusion profiles of both spot mode scans from four different radial directions (A-D) were compared to illustrate the effect that radiation damage has on diffusion length. The results are shown in Figure 17 below.

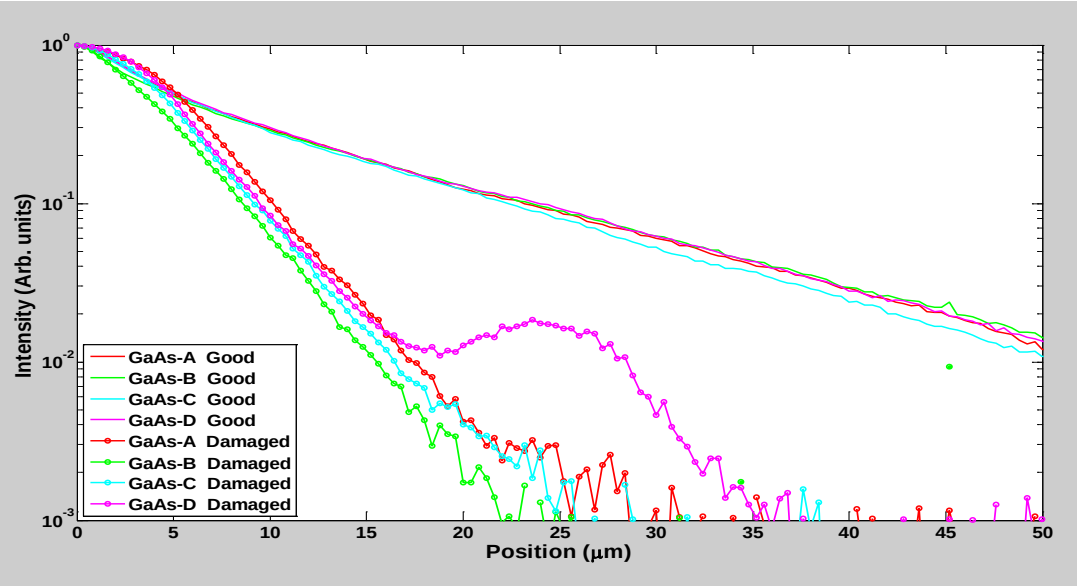

Figure 17. Plot of intensity vs. position showing the shorter diffusion length for the damaged portion of the sample (the purple hump is an artifact of the CCD array camera)

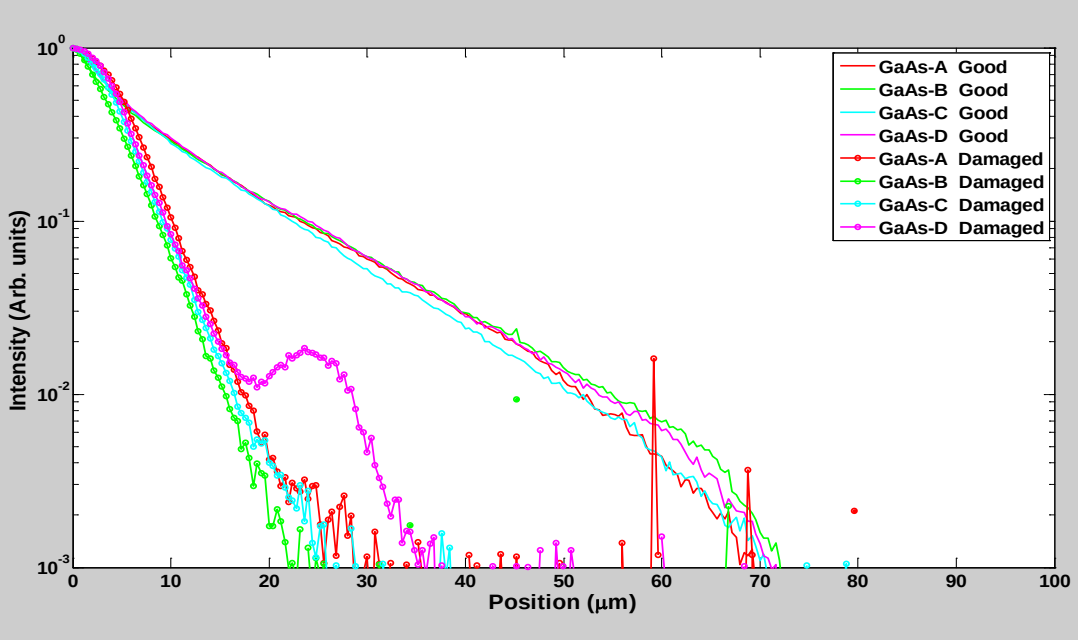

Figure 18. Plot of intensity vs. position showing the longer diffusion length for the uniform portion of the sample

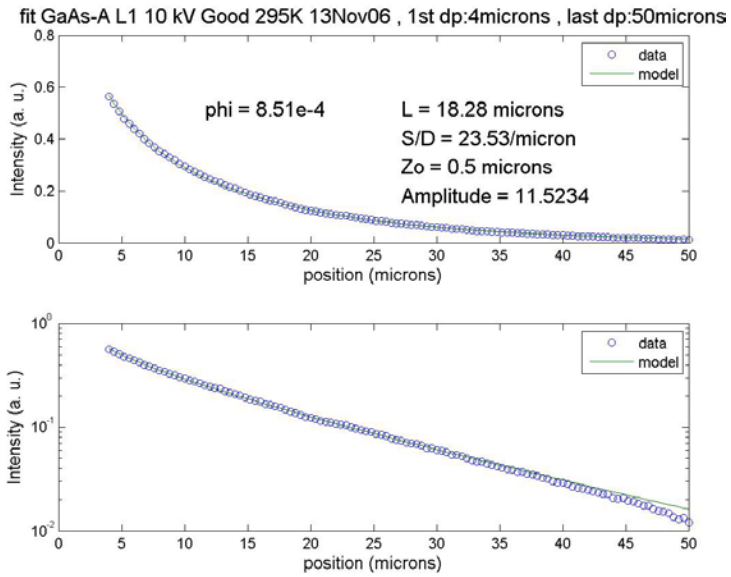

Figure 19. Least squares fit of intensity vs. position showing the longer diffusion length for the uniform portion of the sample

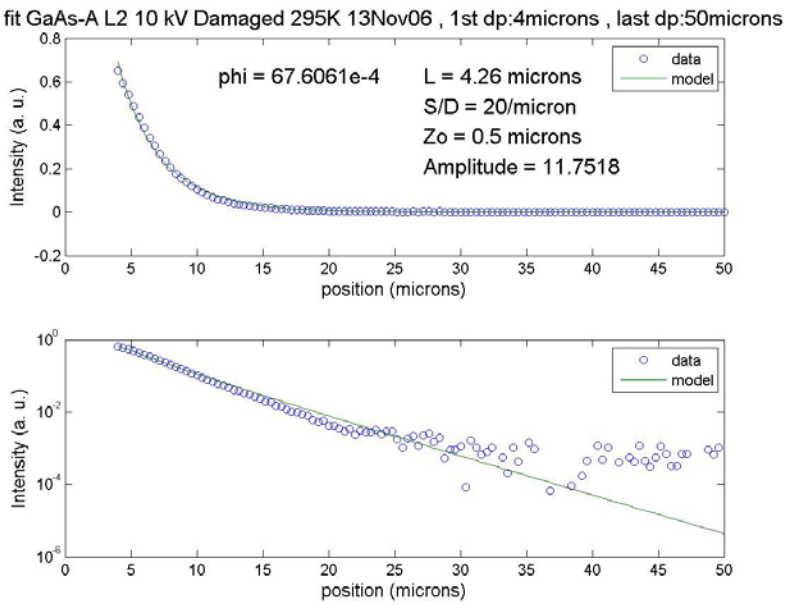

Figure 20. Least squares fit of intensity vs. position showing the shorter diffusion length for the damaged portion of the sample

The results of this experiment illustrate that the data handling and model accurately converts CCD images into data, averages and normalizes peak values, and extracts the relevant material parameters.

THIS PAGE INTENTIONALLY LEFT BLANK

III. EXPERIMENTAL DATA

A. OVERVIEW OF EXPERIMENTAL WORK

The mathematical model derived in Chapter II of this thesis was applied to spatially map the diffusion length L_d and mobility-lifetime ($\mu\tau$) product for two bulk CZT samples. These samples were obtained through collaborations with Brookhaven National Laboratory and Redlen Technologies. The intent of this experimental work was to locate crystal defects in the luminescence maps of both samples, map charge transport properties near these defects, and then use supporting techniques to further investigate the nature of the defects.

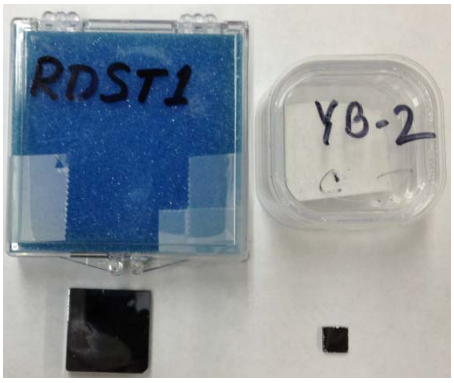

Figure 21. CZT samples RDST1 and YB2

Both samples were initially inspected for defects using a combination of the SEM's picture mode setting and cathodoluminescence (CL) imaging option. Spatial variations in the CL intensity were observed on the sample and further investigated to determine defect geometry and depth below the sample surface. Energy-Dispersive X-ray Spectroscopy (EDS) was then performed to attempt to determine the elemental composition of the defect. Finally, Focused Ion Beam (FIB) milling was performed to remove portions of the sample for a closer look at defect geometry, composition, and depth below the surface. Detailed descriptions of these measurements are provided below.

B. TRANSPORT IMAGING DATA

It is important to note that since CZT is a high-resisitivity semiconductor with very low ($< 10^6$ cm^{-3}) carrier concentrations, electron-hole pair recombination is dominated by the generated carriers, and electrons and holes must diffuse together. Thus, all diffusion length measurements recorded in this thesis for CZT are ambipolar diffusion lengths.

On 30-Aug-12, the RDST1 sample from Redlen Technologies was placed inside the scanning electron microscope and cooled to 5K to increase signal-to-noise ratio and improve image contrast. The sample was then analyzed in the SEM's picture mode, using *10 keV* acceleration voltage, with *3e-10 A* probe current, at *500*× magnification and at *39 mm* working distance for an exposure time of *5 s*. The SEM's picture mode provides a rectangular CL image at the sample surface, indicating spatial variations in intensity and highlighting defective regions that would otherwise appear uniformly bright. Recall that uniformly bright areas of the sample are indicative of uniform EHP recombination, while darker areas of the sample generally suggest that scratches, grain boundaries, and other crystal defects trap EHPs that would otherwise emit recombination luminescence. After a brief search of the RDST1 sample, two dark, triangular-shaped defective regions were located above what appears to be a grain boundary.

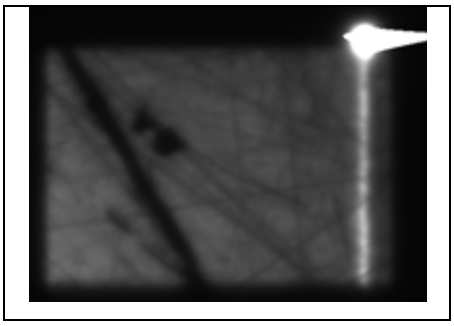

Figure 22. Area luminescence map of RDST1 sample surface (picture mode) showing defects at 500× magnification

Transport imaging was then performed across these two inclusions to determine the spatial variation of the diffusion length near the two defects. A total of 14 vertical

line scans were taken horizontally over the *30 μm* inclusion region at *2 μm* horizontal increments in accordance with the Method 1 technique illustrated in Figure 8. These line scans are depicted graphically in Figure 23. The 14 scans were performed at *10 keV* acceleration voltage, at *1200* × magnification, with probe current of *6e-10 A*, a working distance of *39 mm*, and an exposure time of *120* seconds each. The line scan data was then imported into MATLAB, plotted, and analyzed with the assistance of Kevin Tang, a Physics intern at the Naval Postgraduate School.

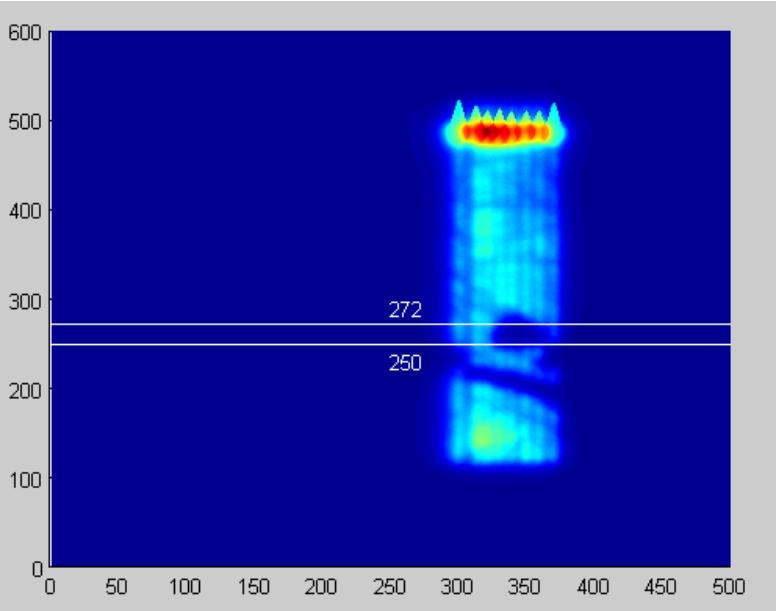

Figure 23. Line scan data imported into MATLAB

The 2-D MATLAB surface plot in Figure 23 indicates intensity [*color*] vs. (x,y) position [*pixels*]. As expected, this plot closely matches the pic-mode image taken earlier in the SEM. A *0.4 μm*-to-pixel conversion reveals the dimensions of one of the defect regions to be approximately *10 μm* ×*10 μm*. The 250-272 pixel (*8.8 μm*) vertical region of each of the 14 line scans was then analyzed using the least squares fit, and the diffusion lengths were plotted for each line scan. Diffusion lengths were observed to increase near the defect.

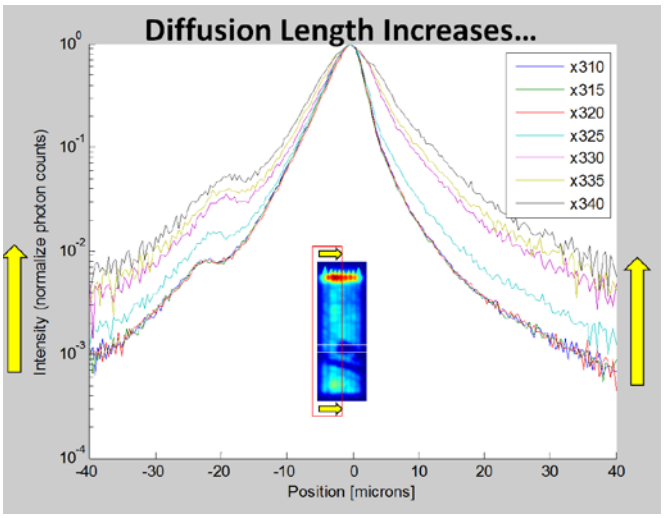

Figure 24. Plots of intensity vs. position for line scans progressing from the left side of the sample to the center of the defect. These diffusion lengths increased near the defect.

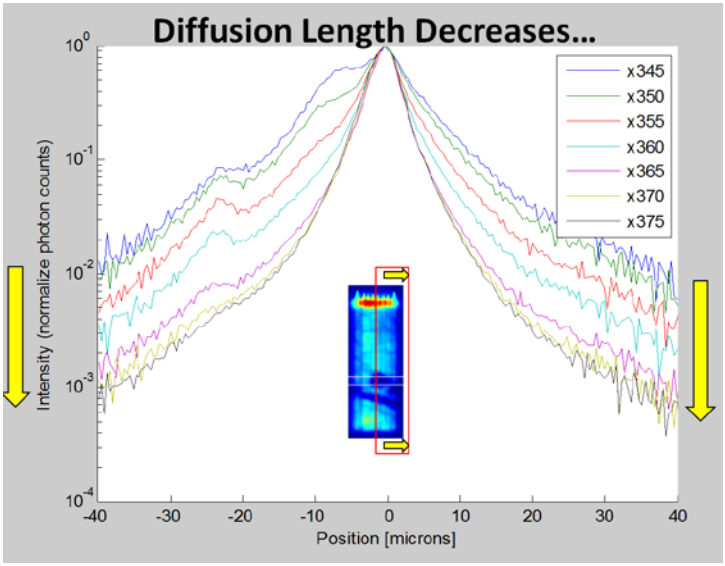

Figure 25. Plots of intensity vs. position for line scans progressing from the center of the defect to the right side of the sample. These diffusion lengths decreased away from the defect.

Figures 24 and 25 depict diffusion length increasing as the transport imaging process approaches a defect. As these line scans continue rightward through the defect, the largest diffusion length values are observed. As the plot in Figure 27 below indicates, the highest diffusion length is measured dead-center (at the *0 μm* position) of the defect,

suggesting that the material in the immediate vicinity of the defect has the best transport properties for minority carriers.

Line	Minimized Sum of Square Residuals Phi	Diffusion Length L_D [micron]	Surface Recomb. Velocity / Diffusivity S/D [1/micron]	Electron Beam Penetration Depth Z_0 [micron]
x310	3.6021e-4	4.24	131.63	0.5
x315	3.0341e-4	4.47	145.8	0.5
x320	2.9561e-4	4.41	139.61	0.5
x325	6.0110e-4	5.68	113.65	0.5
x330	40.4811e-4	6.39	53.09	0.5
x335	56.8611e-4	6.77	47.11	0.5
x340	69.7100e-4	7.24	36.34	0.5
x345	33.7991e-4	9.84	43.00	0.5
x350	28.0461e-4	8.86	50.05	0.5
x355	15.7111e-4	7.49	67.87	0.5
x360	9.6610e-4	6.25	89.09	0.5
x365	4.2151e-4	4.74	112.52	0.5
x370	2.9100e-4	4.23	109.75	0.5
x375	2.0471e-1	4.06	108.85	0.5

Figure 26. Table of diffusion length vs. position for RDST1 sample

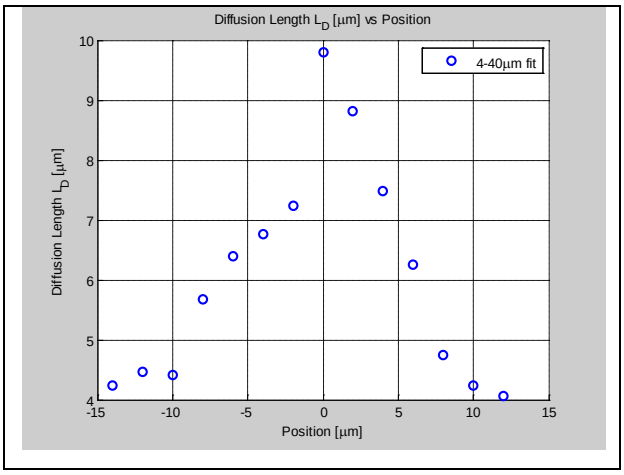

Figure 27. Plot of diffusion length vs. position for RDST1 sample

A similar experiment was conducted for the YB2 sample. On 28-Jan-13, the YB2 sample from Brookhaven National Laboratory was placed inside the scanning electron microscope and cooled to 5K to increase luminescent intensity and improve signal-to-noise ratio. After a brief search in picture mode, four dark, triangular-shaped defects were located. The image in Figure 28 below was taken at *10 keV* electron beam acceleration voltage, *3e-10 A* probe current, *500*× magnification, and a *39 mm* working distance for an exposure time of *4 sec.*

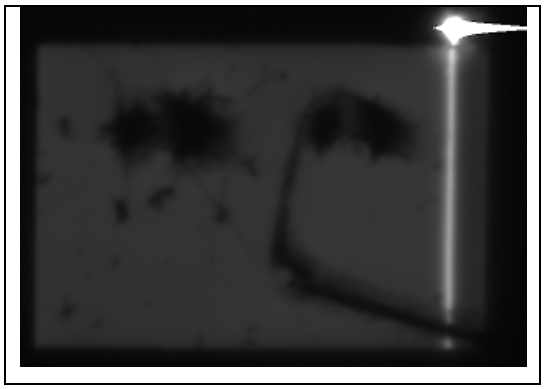

Figure 28. Picture mode scan of YB2 sample surface showing defect regions

Transport imaging was then performed on the sample in accordance with the Method 2 technique previously depicted in Figure 8 to determine the spatial variation of diffusion length near these defects. This was done by taking one line mode scan through all four defects and measuring the diffusion length at multiple sections along the single line scan. The scans were conducted at *10 keV*, *500*× magnification, with probe current of *3e-10 A* and a working distance of *39 mm* at an exposure time of *0.6 sec*. As Figures 29-30 indicate, the line scan data (left) was then imported into MATLAB and compared with a nearby line scan through a more uniform area of the sample (right).

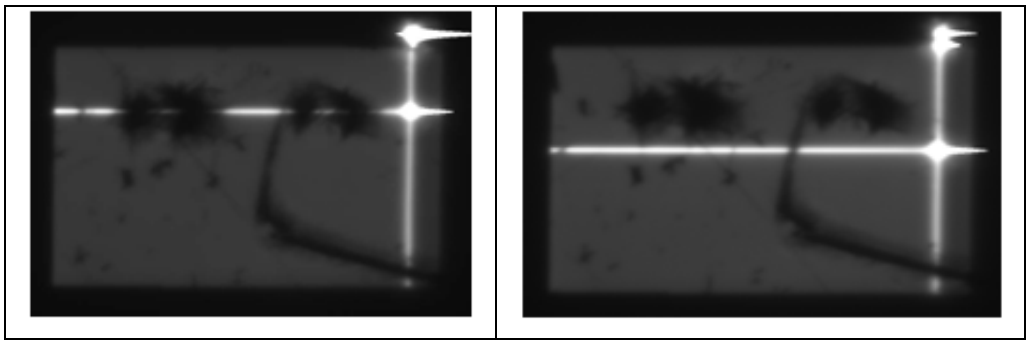

Figure 29. Picture mode/line mode hybrid images of the YB2 sample, indicating a line scan through four defects (left) and a line scan through a more uniform area of the sample (right)

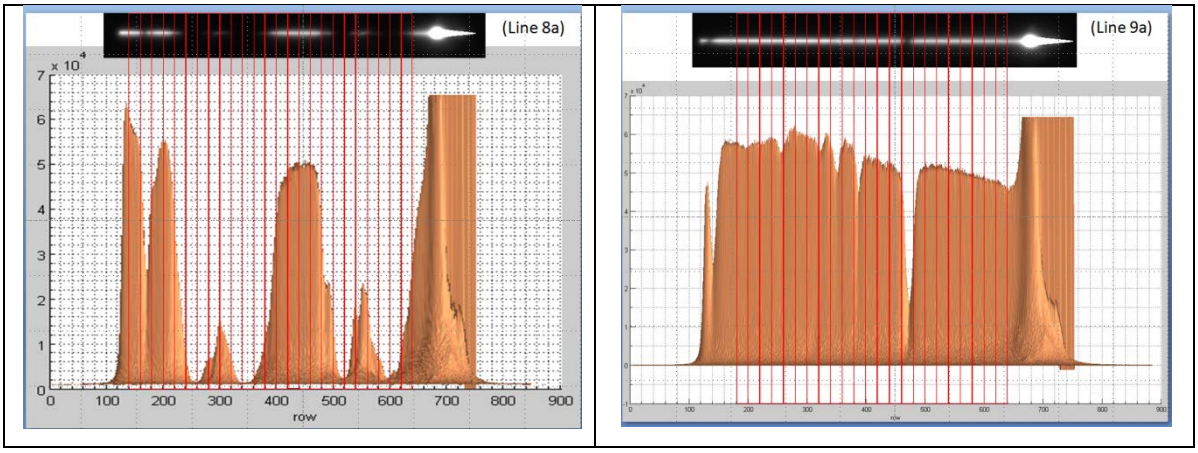

Figure 30. Plots of intensity vs. position for a line mode scan through four defects (left) compared with a line mode scan through a more uniform area of the sample (right)

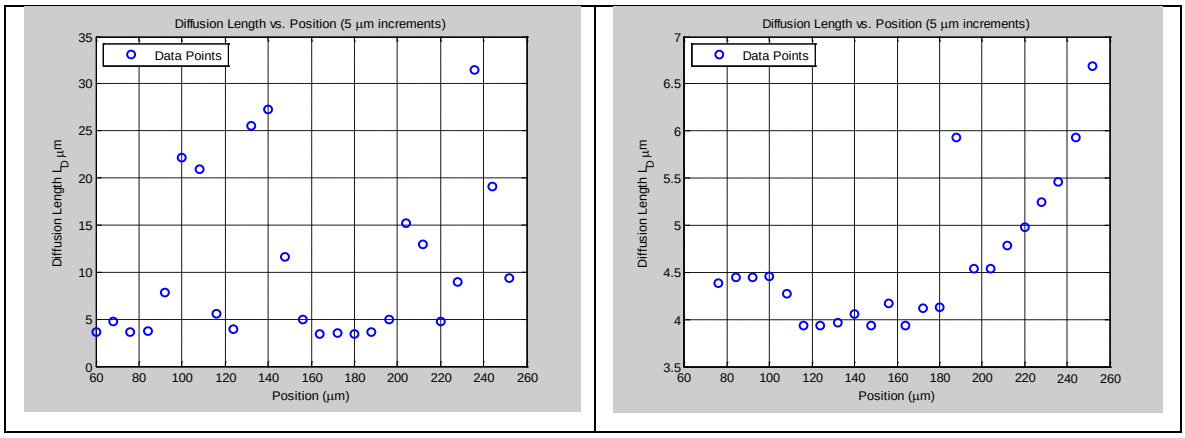

Figure 31. Plots of diffusion length vs. position for a line mode scan through four defects (left) compared with a line mode scan through a more uniform area of the sample (right)

As Figure 31 indicates, the largest diffusion length values were observed near the defects (left), while more gradual diffusion length variations were observed in a line scan conducted away from the inclusion (right).

C. CATHODOLUMINESCENCE DATA

Cathodoluminescence imaging with variable excitation voltage was then performed on the RDST1 sample to estimate defect geometry and depth. As mentioned previously, an increase in the SEM's electron beam acceleration voltage increases the bulbous area of the electron interaction volume and consequently increases the maximum electron beam penetration depth z_0. Mathematical models by Everett and Hoff [15] (Equation 88) and Kanaya and Okayama [16] (Equation 89) have predicted electron beam penetration depths z_o [μm] as a function of the SEM's electron beam acceleration voltage E_b [keV].

$$Z_0 = \left(\frac{0.0398}{\rho} \right) E_b^{1.75} \tag{88}$$

$$Z_0 = \left(\frac{0.0276A}{\rho Z^{0.889}} \right) E_b^{1.67} \tag{89}$$

These two models were used to estimate SEM electron beam penetration depth for the RDST1 and YB2 CZT samples. The following CZT properties were used for these equations:

$$\text{Average atomic weight} \quad A_{avg} = \left\{ \begin{matrix} 112.411 \text{ for Cd } (42.5\%) \\ 65.409 \text{ for Zn } (7.5\%) \\ 127.600 \text{ for Te } (50\%) \end{matrix} \right\} = 116.48 \left[\frac{g}{mol} \right] \tag{90}$$

$$\text{Density of CdTe} \quad \rho_{CdTe} = 6.20 \left[\frac{g}{cm^3} \right] \tag{91}$$

$$\text{Average atomic number} \quad Z_{avg} = \left\{ \begin{matrix} Z_{Cd} = 48 \ \ (42.5\%) \\ Z_{Zn} = 30 \ \ (7.5\%) \\ Z_{Te} = 52 \ \ (50\%) \end{matrix} \right\} = 49 \tag{92}$$

Results for these two models were then plotted for electron beam acceleration voltages ranging from 0-40 *keV* in Figure 32 below. Key voltages of *5*, *10*, *20*, and *30 keV* were highlighted, since these voltages were employed in this thesis to investigate defects beneath the RDST1 sample surface.

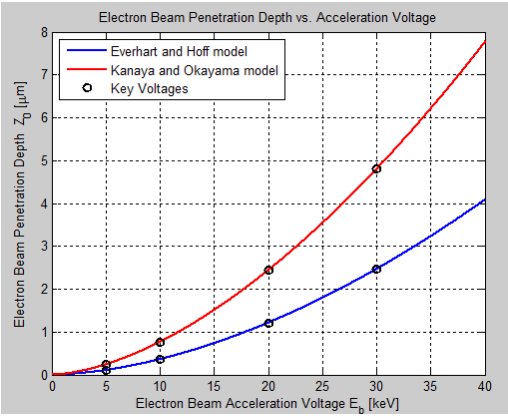

Figure 32. Electron beam penetration depth z_o as a function of electron beam acceleration voltage E_b for CZT.

Ranges of electron beam penetration depths z_o at key voltages were then estimated using the results of Figure 32. These estimated ranges are shown below in Table 2.

Eb	Lower Limit	Upper Limit
5 keV	0.1 µm	0.25 µm
10 keV	0.35 µm	0.75 µm
20 keV	1.2 µm	2.5 µm
30 keV	2.5 µm	4.8 µm

Table 2. Electron beam penetration depths z_o as a function of key electron beam acceleration voltages E_b for CZT.

With these results in mind, the SEM's electron beam acceleration voltage was varied from *5-30 keV* during CL imaging of the CZT defects discovered on the RDST1 sample, with results shown in Figures 33-36 below. Measurements of intensity [*counts*] vs. position [μm] were made for each line scan conducted within each CL image to estimate the dimensions of the two defective areas.

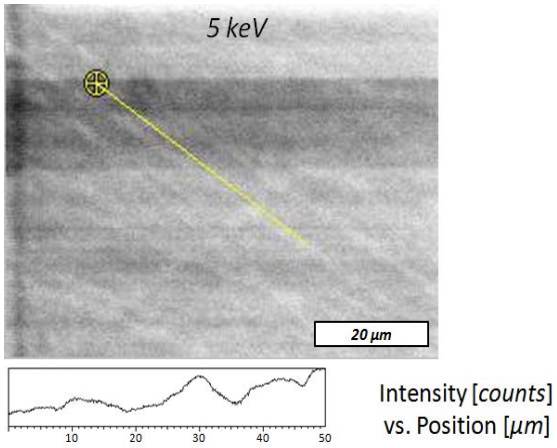

Figure 33. CL image of defects on RDST1 sample at 5 keV at 1500× magnification (electron beam acceleration voltage is too low to show the defects). The yellow line is drawn through both defects for reference, and an intensity vs. position plot is shown below to depict intensity along the yellow line.

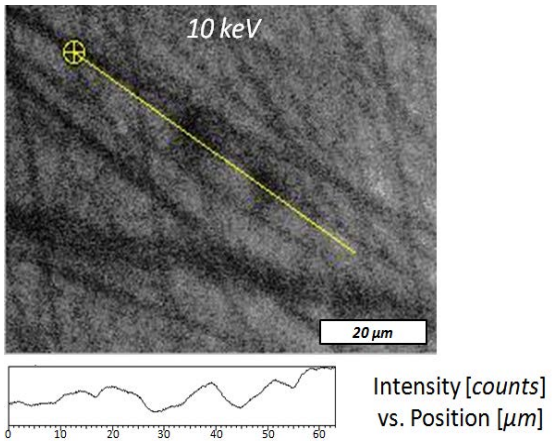

Figure 34. CL image of defects on RDST1 sample at *10 keV* at *1500*× magnification (electron beam acceleration voltage is barely sufficient to show the defects).

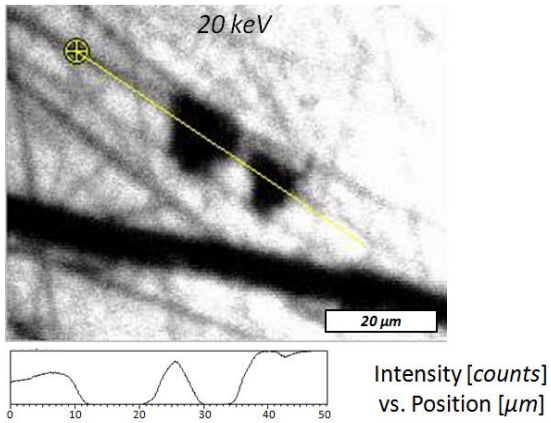

Figure 35. CL image of defects on RDST1 sample at *20 keV* at *1500*× magnification (electron beam acceleration voltage is now sufficient to show significant contrast from the defects).

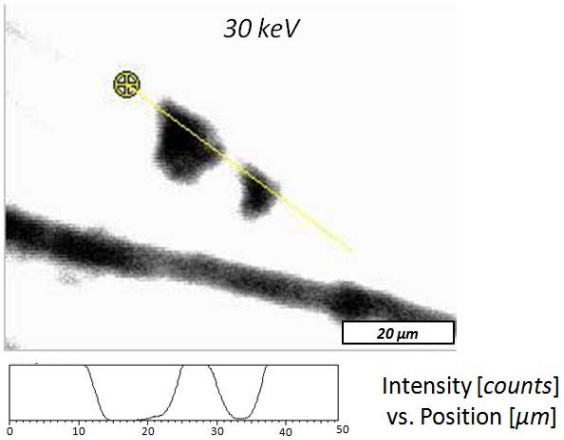

Figure 36. CL image of defects on RDST1 sample at *30 keV* at *1500*× magnification

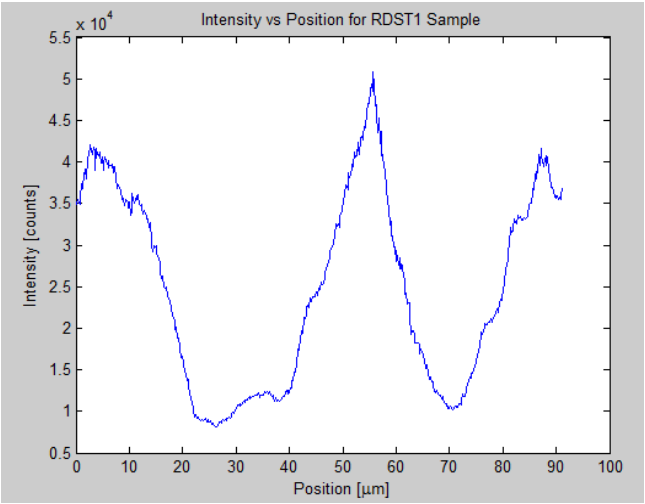

Figure 37. A high-resolution plot of intensity [*counts*] vs position [*µm*] suggests that the diameter of the left defect at full width half max is ~20 *µm.*

Figures 33–36 above depict the luminescence variations associated with defects, which become more apparent as more acceleration voltage is applied. The defects are not visible at *5 keV*, yet at *10 keV*, the defects begin to distinguish themselves from scratches and other defects. At *20 keV*, the defect geometry becomes more pronounced, and at *30 keV*, the contrast is so large that only the inclusions and grain boundary are

distinguishable. These results suggest that the defects lie at least *1-2 μm* below the RDST1 sample surface.

Similar CL imaging techniques were employed to confirm the presence of four defects located on the YB2 sample surface. These images, depicted in Figure 38 below, were taken at *5-10 keV* and *3e-10 A* probe current.

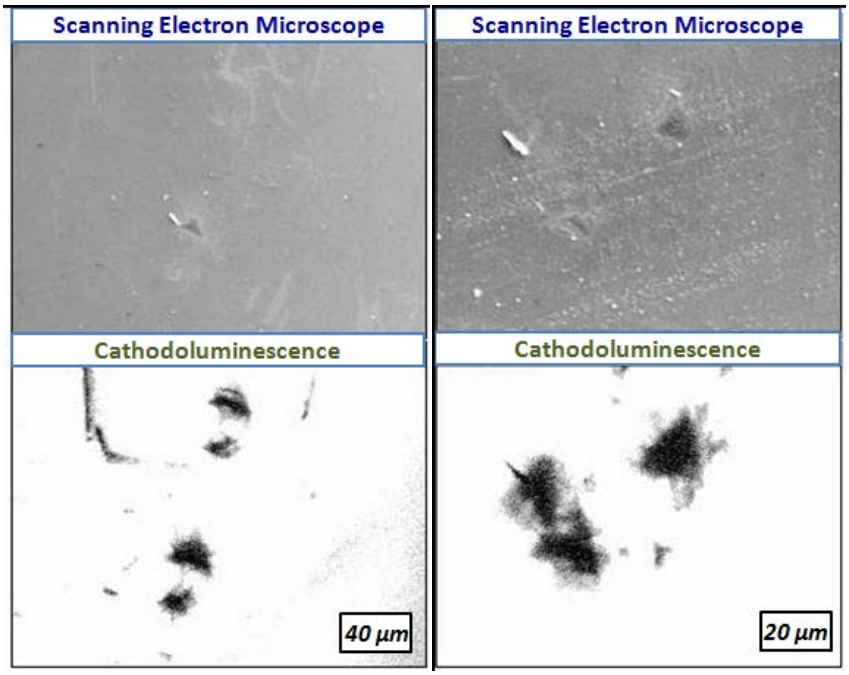

Figure 38. SEM image (above) and CL image (below) of the four previously-analyzed crystal defects (left) and a cluster of three newly-discovered defects in a different area of the sample (right). Both images are from the YB2 sample. The left image was taken at *1000*×, the right at *1500*×

The four defects (left) appeared brightly in CL imaging at *5 keV* and *10 keV*, which suggested that they were closer to the surface than those in the RDST1 sample. The defect shapes seen in CL also appears in the SEM image, which hints of the defect's presence on the surface. For comparison, a separate cluster of defects was located on a different area of the YB2 sample and viewed with CL. Again, the defect geometry evident in CL also appeared in the SEM image, suggesting a second instance of crystal defects located near the sample surface.

D. ENERGY DISPERSIVE X-RAY SPECTROSCOPY

Energy-Dispersive X-ray Spectroscopy (EDS) was then performed to investigate the elemental composition of defects identified in the RDST1 and YB2 samples. EDS is a chemical microanalysis tool that detects and maps x-rays that are emitted as the SEM's electron beam bombards the sample [10]. During this electron beam bombardment, the sample's lower-energy electrons are knocked out of their lower orbits, causing higher-energy electrons to reduce their orbit energy in order to occupy these newly-formed vacancies and achieve equilibrium. As these electrons move from higher to lower orbits, they emit x-rays (K_α, K_β, L_α) characteristic of the orbit energies, which can be collected via the EDS detector and plotted as peaks in an X-ray spectrum to help identify the sample's elemental composition.

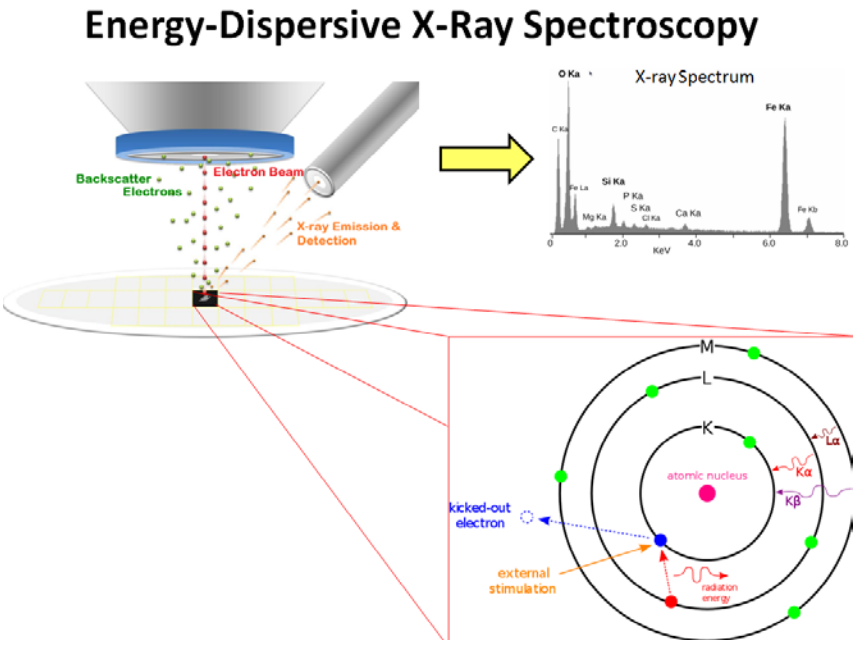

Figure 39. Energy-Dispersive X-Ray Spectroscopy diagram, showing the bombardment of a sample by an electron beam, which causes the emission of characteristic x-rays collected by the EDS detector and converted into an X-ray spectrum [10].

The RDST1 sample was analyzed first. The EDS process was conducted on a more uniform area of the sample and compared with an EDS spectra obtained from the

two triangular-shaped defects previously identified in CL (Figure 35) and mapped with transport imaging. These measurements were conducted at *10 keV* for approximately 20 minutes. The results are shown in Figure 40.

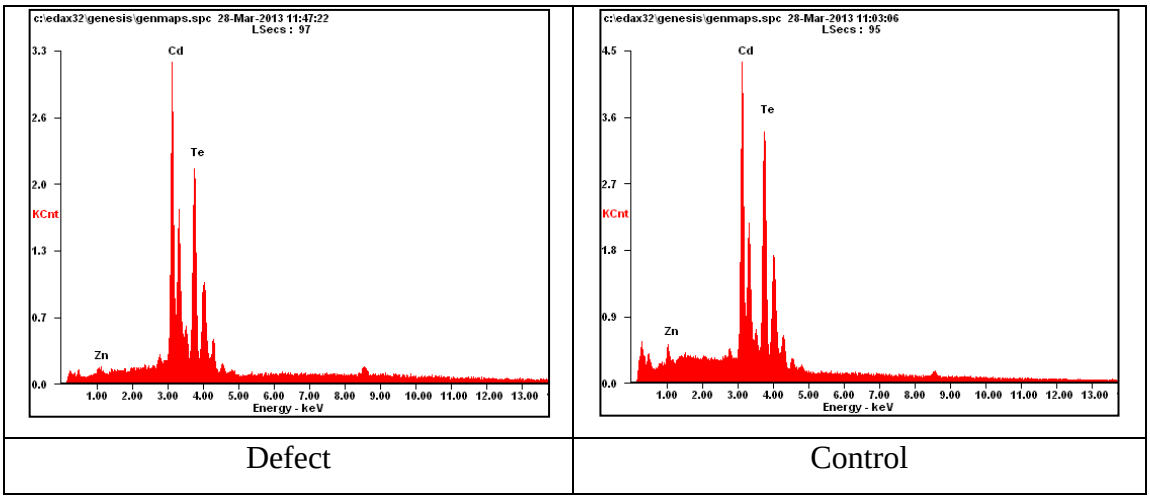

Defect | Control

Figure 40. Energy spectrum for defect (left) and control region (right) on the RDST1 sample

The resulting spectra did not differ enough to indicate a significantly different concentration of Te or Cd within the defect area, though it is important to note that both spectra reflect the expected $Cd_{1-x}Zn_xTe$ relationship, with the $0.1 \le x \le 0.2$ percentage of Zn. X-ray mapping of the RDST1 defective region was then performed by rastering the SEM beam across a square area of the sample and collecting the resulting x-rays. This experiment was conducted in a method similar to CL area imaging, though this time, spatial variations in the concentrations of Cd, Zn, or Te elements within the CZT material were mapped.

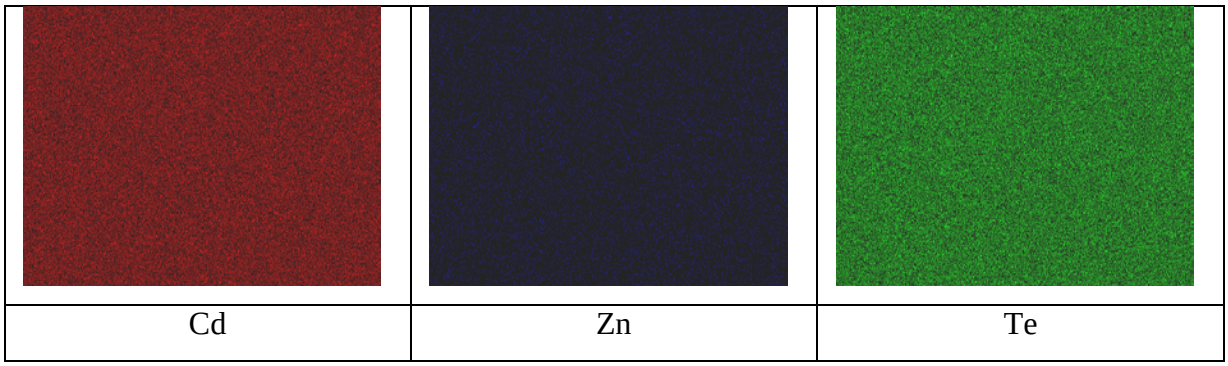

Figure 41. EDS spatial mapping of the RDST1 defect area, showing uniform concentrations of Cd (red), Zn (blue), and Te (green)

No significant localized variations were observed in the maps in Figure 41, which suggested that even though defects were observed in CL, either these defects were too deep below the sample surface for the characteristic x-rays to be detected or the defects were too small to be resolved by the detector. This EDS process was repeated with the YB2 sample, since the results of CL area mapping suggested that the defects were closer to the surface. However the same results were observed, suggesting either that the defects were not composed of excess Te or Cd, or that they are too small to be identified in an EDS mapping of the defect area.

E. FOCUSED ION BEAM MILLING

To gain a better understanding of the nature of the defects within the RDST1 sample, Focused Ion Beam (FIB) milling was employed to remove portions of the defective area in sub-micron slices so that the area beneath the surface could be exposed and inspected.

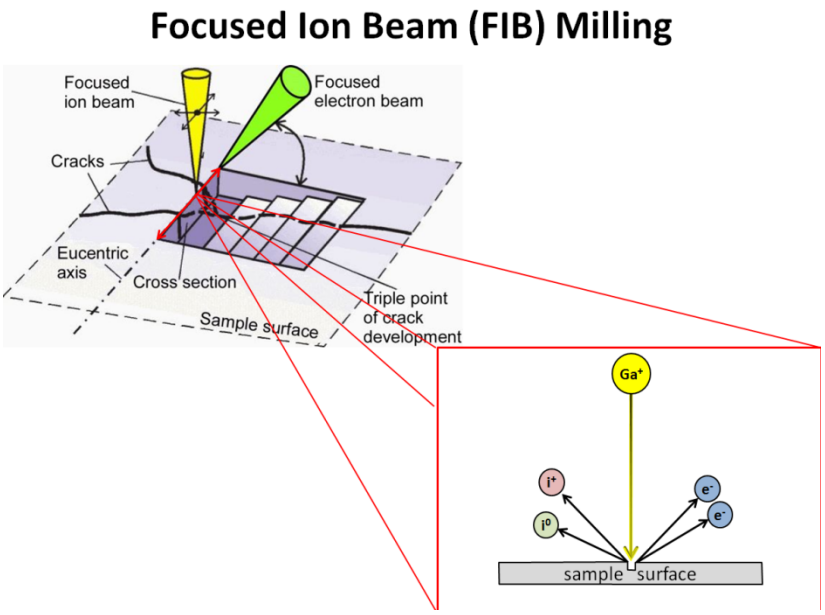

Figure 42. Focused Ion Beam (FIB) Milling diagram (top right), showing the focused gallium ion beam (yellow) rastering back and forth to sputter away *30 μm*-deep slices of the sample at an angle orthogonal to the sample surface. The sputtering diagram (bottom left) shows the gallium ion beam (yellow) bombarding the sample, causing atoms from the sample to be ejected as secondary ions, neutral atoms, or secondary electrons. After [11–12].

FIB milling employs a highly-concentrated, well-focused gallium ion beam to sputter away portions of the sample at an angle orthogonal to the sample surface. Sputtering occurs upon interaction of the gallium ion beam with the sample surface, since the kinetic energy of the accelerated gallium ions exceeds the surface binding energy of atoms on the sample surface. As a result of this interaction, charged atoms on the sample surface are ejected from the ion beam point of impact in addition to secondary ions, secondary electrons, etc. Since sputtering occurs at the atomic order of magnitude, FIB milling can be highly-precise method to slice away sub-micron sections of a sample's surface. Note that since the FIB beam is at a 54° angle in relation to the electron beam in the Zeiss Neon 40 EsB FIB/SEM beam as depicted in Figure 42, slices of the sample must initially be removed in a stair-step pattern in order to allow the SEM beam to access the newly-exposed cross-sectional area of the sample for imaging.

Figure 43 below depicts SEM and CL images of the RDST1 CZT sample taken before and after every FIB milling slice to detect the slightest variation in material properties that would confirm the presence or absence of a sub-surface crystal defect.

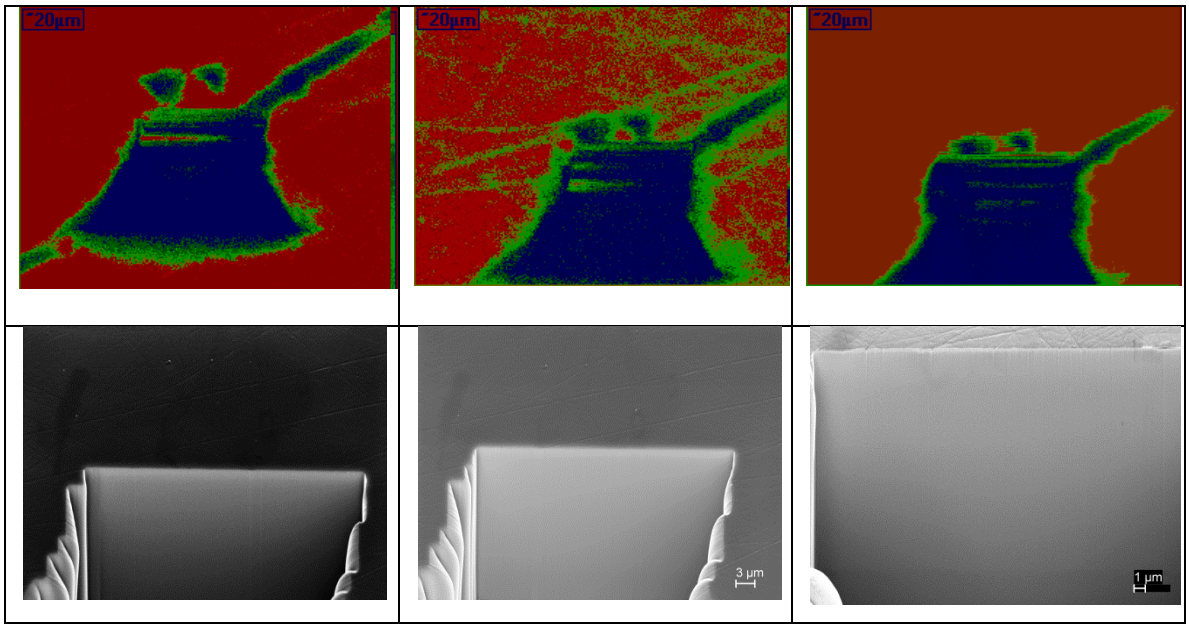

Figure 43. False-color CL imaging (top three) taken normal to the sample surface, and SEM imaging (bottom three) of the same area, taken at a 45° angle with respect to the CL image. The trapezoidal dark regions of the CL images are the stair-step etching patterns necessary to expose the cross-sectional sample area to the SEM beam for imaging. Images from left to right show progressive milling upwards towards the center of the two crystal defects. Red represents high intensity, while blue represents low intensity.

Note the stair-step pattern of slices that appear as trapezoidal black shapes in the top three CL images of Figure 43. These incremented slices, beginning at the bottom of the image and working their way to the top, were necessary to expose the *30 µm*-deep cross-sectional area to the SEM beam for imaging. Note the bottom three SEM images in Figure 41show no sub-surface defects.

An SEM picture of the exposed cross-sectional area was taken after every sub-micron-thick slice of material was removed. This process continued until four defects were finally spotted beneath the sample surface, at a point where 50% of the leftmost

crystal defect had been milled away. The defects range from 3 μm to*15* μm beneath the sample surface, which agree with the predictions in Table 2 and Figure 32.

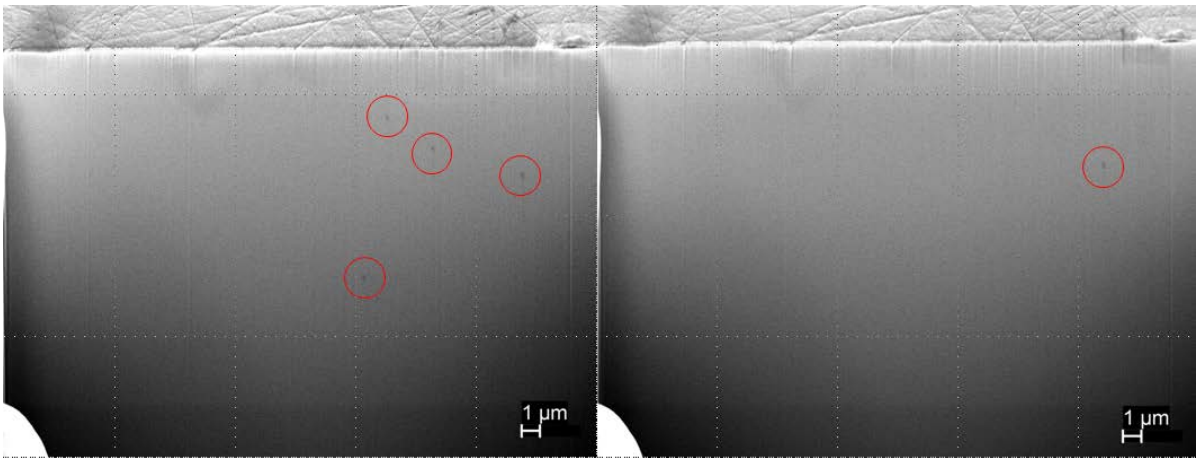

Figure 44. SEM image of RDST1 sample in FID area showing defects

One more 0.5 μm slice of CZT was milled away, and three of the four defects disappeared, yet one defect 5 μm beneath the sample surface remained visible. EDS was then performed on the location of the remaining defect to determine its composition. A control measurement was also taken for comparison.

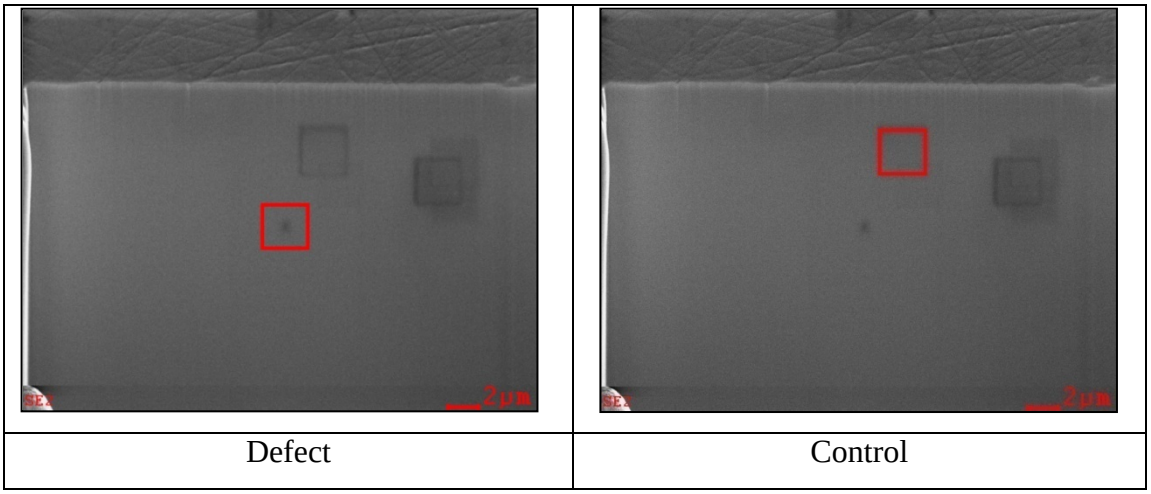

Figure 45. EDS performed on defect area and compared with more uniform portion (control area) of the RDST1 sample

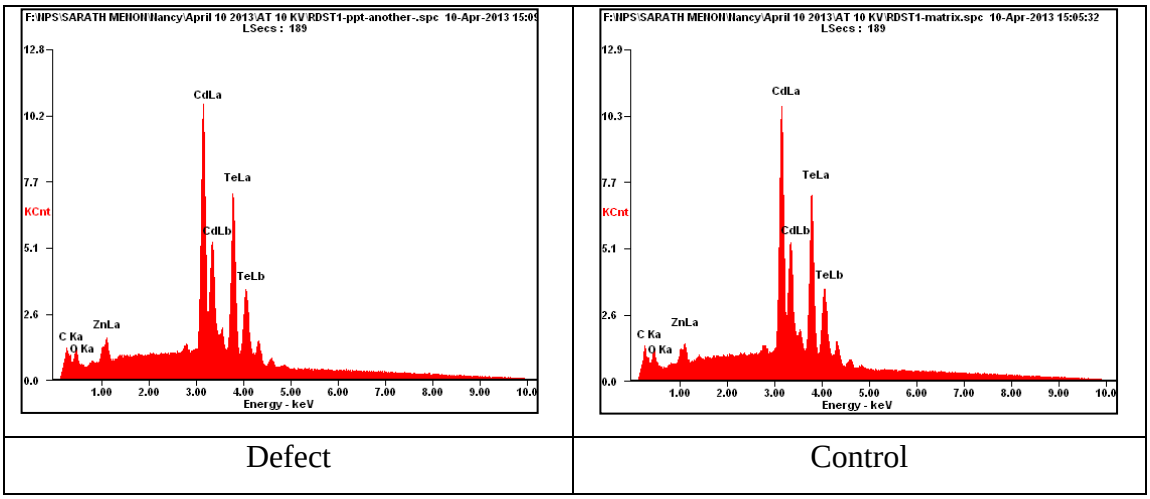

Figure 46. Energy spectrum comparison of defect area and uniform portion (control area) of the RDST1 sample highlighted in Figure 43.

As observed earlier, the resulting spectra did not differ enough to indicate a significant concentration of Te or Cd within the defect area. X-ray mapping of the RDST1 defect area in Figure 44 was then performed in order to highlight any concentrations of Te or Cd in the vicinity of the defect.

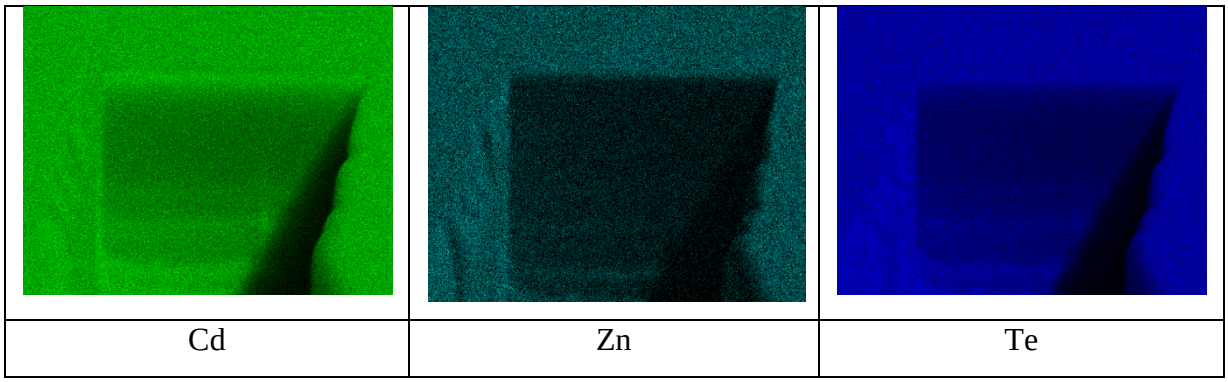

Figure 47. EDS spatial mapping of the FIB-milled RDST1 defect area, showing uniform concentrations of Cd (red), Zn (green), and Te (blue)

No significant localized variations were observed in the maps in Figure 47, which confirms what was suggested earlier—that even though defects were seen in the cross-sectional SEM image of the sub-surface sample area, they were too small to be resolved by EDS. This makes sense, since most EDS sensors are unable to resolve elemental

concentrations below the micron level of resolution. However, it is interesting to note that such a small (0.25 μm diameter) defect is capable of affecting recombination luminescence in such a large (20 μm diameter) area of the sample as the CL experiments observed.

E. THE PHYSICS BEHIND THESE EXPERIMENTAL RESULTS: ONE POSSIBLE EXPLANATION

Transport imaging of the defect areas in the RDST1 and YB2 samples revealed increasing diffusion lengths in the vicinity of crystal defects. This is initially counterintuitive, since one would expect the diffusion lengths to decrease in areas where recombination luminescence decreased. However, this observation can also be explained mathematically by carefully considering the relationship between lifetime and luminescence intensity. First, several equations must be introduced.

Recall Equation (6), which gave diffusion length L_d as a function of a material's mobility μ and lifetime τ. This equation indicates that increases in L_d must come from increases in the $\mu\tau$ product.

$$L_d = \sqrt{\frac{kT}{e}\mu\tau} \tag{6}$$

The lifetime τ in Equation 6 is actually the effective lifetime τ_{eff} [s] which is composed of two elements: radiative carrier lifetime τ_{rad} [s], and non-radiative carrier lifetime $\tau_{non-rad}$ [s]. The relationship between τ_{eff}, τ_{rad}, and $\tau_{non-rad}$ is shown in Equation (93) below.

$$\frac{1}{\tau_{eff}} = \frac{1}{\tau_{rad}} + \frac{1}{\tau_{non-rad}} \tag{93}$$

Radiative lifetime τ_{rad} can also be written in terms of a relationship between dopant concentration $n_{dopants}$ [$1/m^3$] and proportionality constant B [$1/m^3 s$] with the following equation.

$$\tau_{rad} = \frac{B}{n_{dopants}} \tag{94}$$

Recombination luminescent intensity is defined by Equation (91), where I is intensity [*arbitrary units*], G is the carrier generation rate [*carriers/s*], τ_{eff} is the effective carrier lifetime [*s*], and τ_{rad} is the radiative lifetime [*s*].

$$I \sim \frac{G\tau_{eff}}{\tau_{rad}} \tag{95}$$

It is useful to analyze the limits of the above three equations for a better understanding of semiconductor luminescence phenomena. For doped semiconductors where $n_{dopants}$ becomes large, τ_{rad} becomes small. This value of τ_{rad} is also small compared to $\tau_{non-rad}$, thus $\tau_{rad} << \tau_{non-rad}$. At this limit, the $\frac{1}{\tau_{non-rad}}$ term in Equation (93) becomes negligible, rendering $\frac{1}{\tau_{eff}} = \frac{1}{\tau_{rad}}$, which simplifies to $\tau_{eff} \approx \tau_{rad}$. Thus, by Equation (91), the intensity I becomes equal to the magnitude of the charge carrier generation rate G, or $I \to G$. This high efficiency of radiative recombination explains why doped semiconductors often appear brighter in CL imaging.

The other limit may exist for undoped semiconductors. In the undoped case, where the $n_{dopants}$ term becomes smaller, τ_{rad} becomes large. If this value of τ_{rad} is also large compared to $\tau_{non-rad}$, then $\tau_{rad} >> \tau_{non-rad}$. At this limit, the $\frac{1}{\tau_{rad}}$ term in Equation (93) becomes negligible, rendering $\frac{1}{\tau_{eff}} = \frac{1}{\tau_{non-rad}}$, which simplifies to $\tau_{eff} \approx \tau_{non-rad}$. Thus, by Equation (95), the intensity I generally approaches zero, or $I \to 0$. Though this is an extreme case, it does explain why undoped semiconductors with a high level of non-radiative recombination appear less bright in CL imaging. A graphical depiction of this limit analysis of Equation (89) is depicted in Figure 46 below.

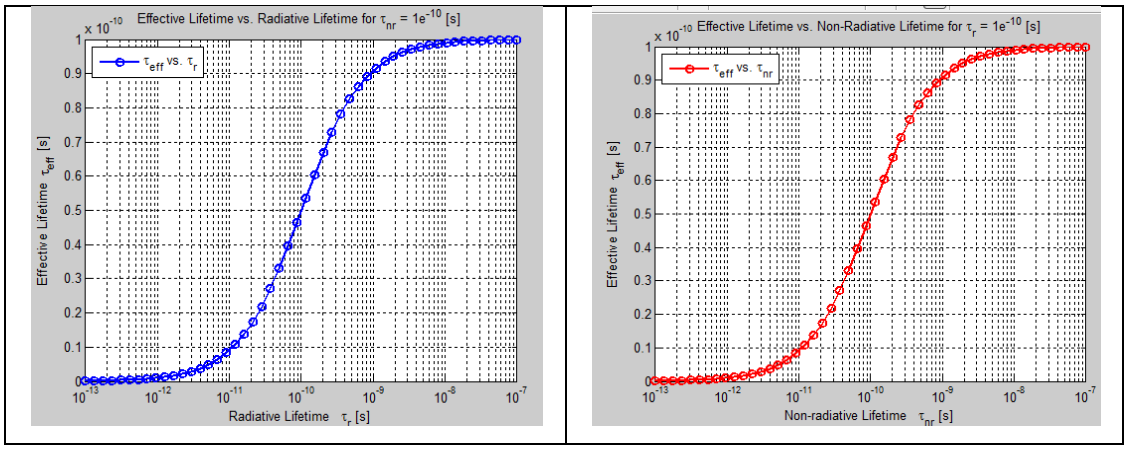

Figure 48. Limit analysis of Equation (89) for fixed $\tau_{non-rad} = 1 \times 10^{-10}$ (left) and for fixed $\tau_{rad} = 1 \times 10^{-10}$ (right). These plots depict effective lifetime as a function of radiative lifetime (left) or non-radiative lifetime (right).

Crystal defects within a semiconductor, such as those studied in this thesis, trap free charge carriers and provide low-energy sites for non-radiative recombination. Charge carriers hindered by these crystal defects would otherwise emit recombination luminescence. Since an increase in material dopants is known to increase the number of free charge carriers, then logically, the inverse must also be true. That is, the reduction of dopants must result in fewer free charge carriers. Since crystal defects essentially reduce the number of otherwise unhindered free charge carriers, the presence of defects can be equated with a reduction of dopants. By this rationale, the presence of crystal defects follows the limit analysis of Equation (93) for undoped semiconductors, where $\tau_{eff} \approx \tau_{non-rad}$ and by Equation (95), the intensity I generally approaches zero, or $I \to 0$. This explains the transport imaging phenomenon of diffusion length increasing around defect areas in both the RDST1 and YB2 samples, where recombination luminescence was comparatively low.

This is a satisfactory conclusion for why diffusion lengths increase near crystal defects, but it does not explain how such a small (0.25 μm diameter) defect is capable of reducing recombination luminescence in such a large (20 μm diameter) area of the sample as the CL experiments observed.

In a publication entitled "Impurity gettering effect of Te inclusions in CdZnTe single crystals," G. Yang et. al. discuss how as the CZT crystal is cooled following the High-Pressure Bridgeman Method, tellurium precipitates out of the matrix and migrates towards low-energy locations within the CdZnTe matrix. As this excess tellurium migrates towards a point defect, the surrounding region becomes more pure. A depiction of this gettering process appears below in Figure (49).

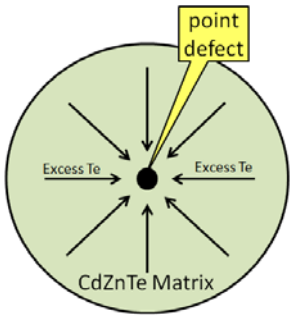

Figure 49. Gettering of excess tellurium towards a point defect within the CdZnTe matrix as the CZT crystal cools.

The spherical geometry of this gettering process can be modeled with Equation (96) below, which relates volume and concentration. Recall that the volume of the sphere is represented by Equation (97).

$$V = \frac{4}{3}\pi r^3 \tag{96}$$

$$V_{dark\ region} \cdot n_{excess} = V_{defect} \cdot n_{te} \tag{97}$$

Equation (93) requires the concentration of tellurium in solid form n_{te}, which is 2.94×10^{22} $[1/cm^3]$, and the typical concentration of excess tellurium n_{excess}, within a CZT crystal, which is 3.00×10^{17} $[1/cm^3]$ [12-13]. Given Equation (97), one can calculate the actual defect diameter beneath the sample surface with the diameter of reduced luminescence appearing on the sample surface and vice versa. In the RDST1 case, the dark triangular pattern observed in CL imagery (Figure 35) was measured to be ~23 μm in diameter, or 11.5 μm in radius. By Equation (93), the defect radius is found to be ~0.25 μm, which agrees with the defect size discovered in Figure 44.

IV. CONCLUSIONS AND AREAS FOR FUTURE RESEARCH

A. CONCLUSIONS

This thesis has demonstrated experimentally that diffusion length increases in areas near the specific crystal defects studied in CZT, where recombination luminescence is comparatively lower than in other areas of the sample. This was shown experimentally via transport imaging as the diffusion lengths were measured in defective areas of two CZT crystals and compared with other more uniform areas of the sample. CL imaging was then used to view spatial recombination luminescence as a function of acceleration voltage, which suggested that defects in the RDST1 sample were several microns below the sample surface and defects in the YB2 sample were somewhat closer to the surface. EDS was unable to confirm the presence of significant Cd, Zn, or Te concentrations within the defective areas of both samples. FIB milling did eventually locate several 0.25 μm diameter defects below the surface, which suggests why EDS was unable to resolve the defects.

Mathematically, the transport imaging model was optimized to eliminate the need for infinite integration, which allowed the analyst to perform the numerical integration of the two Bessel functions in Equation (61) more quickly and with less error. An independent least-squares fitting algorithm was also developed to validate previous transport imaging efforts. Results of the previously-developed Levenberg-Marquardt least-squares algorithm were compared with the Newton's method least-squares algorithm developed in this thesis. Though Newton's method converged much more quickly, the algorithm was prone to converge on local minimums instead of global minimums, yielding erroneous results for certain input values. The Levenberg-Marquardt algorithm, by contrast, was much more reliably convergent, regardless of input values.

B. FUTURE WORK

FIB milling proved effective at discovering defect areas within CZT that had been discovered during CL imaging. However, EDS proved ineffective at characterizing the nature of the defect. At this point, it is unknown whether these defects are concentrations of tellurium, cadmium, zinc, or other elements. More precise, high-resolution imaging methods, such as transmission electron microscopy are needed to determine the composition of these sub-surface defects once they are located. Perhaps in the future, more CZT samples could be obtained, along with the permission to mill the sample surface away and discover more impurities beneath the surface.

Mathematically, the transport imaging least squares data-fitting algorithm can be improved with a modified Armijo rule to adjust descent step sizes accordingly in order to provide a more accurate fit to the data. Modifications to the model could be made in order to analyze the Dirichlet or Neumann boundary conditions for surface recombination velocity parameter S. Variables V and/or Z_o terms could be held constant in the model to analyze changes in other parameters.

APPENDIX EXACT FIRST AND SECOND ORDER PARTIAL DERIVATIVES OF MATH MODEL EQUATION

First-order and second-order partial derivatives of Equation (61) are illustrated below in detail.

$$\frac{\partial u_{\text{model}}(x)}{\partial B} = \int_{-z_0}^{0} K_0\left(\frac{\sqrt{(u+z_0)^2+x^2}}{L}\right)du + \int_{0}^{\infty} e^{-Vu} K_0\left(\frac{\sqrt{(u+z_0)^2+x^2}}{L}\right)du \tag{A1}$$

$$\frac{\partial u_{\text{model}}(x)}{\partial L} = B\left[\int_{-z_0}^{0} K_1\left(\frac{\sqrt{(u+z_0)^2+x^2}}{L}\right)\left(\frac{\sqrt{(u+z_0)^2+x^2}}{L^2}\right)du + \int_{0}^{\infty} e^{-Vu} K_1\left(\frac{\sqrt{(u+z_0)^2+x^2}}{L}\right)\left(\frac{\sqrt{(u+z_0)^2+x^2}}{L^2}\right)du\right] \tag{A2}$$

$$\frac{\partial u_{\text{model}}(x)}{\partial V} = -B\left[\int_{0}^{\infty} u e^{-Vu} K_0\left(\frac{\sqrt{(u+z_0)^2+x^2}}{L}\right)du\right] \tag{A3}$$

$$\frac{\partial u_{\text{model}}(x)}{\partial Z_0} = B\left[K_0\left(\frac{x}{L}\right) - \int_{-z_0}^{0} K_1\left(\frac{\sqrt{(u+z_0)^2+x^2}}{L}\right)\left(\frac{u+z_0}{L\sqrt{(u+z_0)^2+x^2}}\right)du - \int_{0}^{\infty} e^{-Vu} K_1\left(\frac{\sqrt{(u+z_0)^2+x^2}}{L}\right)\left(\frac{u+z_0}{L\sqrt{(u+z_0)^2+x^2}}\right)du\right] \tag{A4}$$

The following exact second-order partial derivatives are used for the Hessian equation (75)

$$\boxed{\frac{\partial^2 u_{\text{model}}(x)}{\partial B^2} = 0} \tag{A5}$$

$$\boxed{\frac{\partial^2 u_{\text{model}}(x)}{\partial L \partial B} = \left[\begin{array}{l} \int_{-z_0}^{0} K_1\left(\frac{\sqrt{(u+z_0)^2+x^2}}{L}\right)\left(\frac{\sqrt{(u+z_0)^2+x^2}}{L^2}\right) du \\ + \int_{0}^{\infty} e^{-Vu} K_1\left(\frac{\sqrt{(u+z_0)^2+x^2}}{L}\right)\left(\frac{\sqrt{(u+z_0)^2+x^2}}{L^2}\right) du \end{array} \right]} \tag{A6}$$

$$\boxed{\frac{\partial^2 u_{\text{model}}(x)}{\partial V \partial B} = -\int_{0}^{\infty} u e^{-Vu} K_0\left(\frac{\sqrt{(u+z_0)^2+x^2}}{L}\right) du} \tag{A7}$$

$$\boxed{\frac{\partial^2 u_{\text{model}}(x)}{\partial Z_0 \partial B} = \left[\begin{array}{l} K_0\left(\frac{x}{L}\right) \\ - \int_{-z_0}^{0} K_1\left(\frac{\sqrt{(u+z_0)^2+x^2}}{L}\right)\left(\frac{u+z_0}{L\sqrt{(u+z_0)^2+x^2}}\right) du \\ - \int_{0}^{\infty} e^{-Vu} K_1\left(\frac{\sqrt{(u+z_0)^2+x^2}}{L}\right)\left(\frac{u+z_0}{L\sqrt{(u+z_0)^2+x^2}}\right) du \end{array} \right]} \tag{A8}$$

$$\boxed{\frac{\partial^2 u_{\text{model}}(x)}{\partial B \partial L} = \left[\begin{array}{l} \int_{-z_0}^{0} K_1\left(\frac{\sqrt{(u+z_0)^2+x^2}}{L}\right)\left(\frac{\sqrt{(u+z_0)^2+x^2}}{L^2}\right) du \\ + \int_{0}^{\infty} e^{-Vu} K_1\left(\frac{\sqrt{(u+z_0)^2+x^2}}{L}\right)\left(\frac{\sqrt{(u+z_0)^2+x^2}}{L^2}\right) du \end{array} \right]} \tag{A9}$$

$$\frac{\partial^2 u_{\text{model}}(x)}{\partial L^2} = B\left[\begin{array}{l} \int_{-z_0}^{0} K_0\left(\frac{\sqrt{(u+z_0)^2+x^2}}{L}\right)\left(\frac{\left|(u+z_0)^2+x^2\right|}{L^4}\right)du \\ -\int_{-z_0}^{0} K_1\left(\frac{\sqrt{(u+z_0)^2+x^2}}{L}\right)\left(\frac{\sqrt{(u+z_0)^2+x^2}}{L^3}\right)du \\ +\int_{0}^{\infty} e^{-Vu} K_0\left(\frac{\sqrt{(u+z_0)^2+x^2}}{L}\right)\left(\frac{\left|(u+z_0)^2+x^2\right|}{L^4}\right)du \\ -\int_{0}^{\infty} e^{-Vu} K_1\left(\frac{\sqrt{(u+z_0)^2+x^2}}{L}\right)\left(\frac{\sqrt{(u+z_0)^2+x^2}}{L^3}\right)du \end{array}\right] \quad \text{(A10)}$$

$$\frac{\partial^2 u_{\text{model}}(x)}{\partial V \partial L} = -B\left[\int_{0}^{\infty} u e^{-Vu} K_1\left(\frac{\sqrt{(u+z_0)^2+x^2}}{L}\right)\left(\frac{\sqrt{(u+z_0)^2+x^2}}{L^2}\right)du\right] \quad \text{(A11)}$$

$$\frac{\partial^2 u_{\text{model}}(x)}{\partial Z_0 \partial L} = \left[\begin{array}{l} K_0\left(\frac{x}{L}\right)\left(\frac{x}{L^2}\right) \\ -\int_{-z_0}^{0} K_0\left(\frac{\sqrt{(u+z_0)^2+x^2}}{L}\right)\left(\frac{u+z_0}{L^3}\right)du \\ -\int_{0}^{\infty} e^{-Vu} K_0\left(\frac{\sqrt{(u+z_0)^2+x^2}}{L}\right)\left(\frac{u+z_0}{L^3}\right)du \end{array}\right] \quad \text{(A12)}$$

$$\frac{\partial^2 u_{\text{model}}(x)}{\partial B \partial V} = -\int_{0}^{\infty} u e^{-Vu} K_0\left(\frac{\sqrt{(u+z_0)^2+x^2}}{L}\right)du \quad \text{(A13)}$$

$$\frac{\partial^2 u_{\text{model}}(x)}{\partial L \partial V} = -B\left[\int_{0}^{\infty} u e^{-Vu} K_1\left(\frac{\sqrt{(u+z_0)^2+x^2}}{L}\right)\left(\frac{\sqrt{(u+z_0)^2+x^2}}{L^2}\right)du\right] \quad \text{(A14)}$$

$$\frac{\partial^2 u_{\text{model}}(x)}{\partial V^2} = B\left[\int_0^{\infty} u^2 e^{-Vu} K_0\left(\frac{\sqrt{(u+z_0)^2+x^2}}{L}\right)du\right] \tag{A15}$$

$$\frac{\partial^2 u_{\text{model}}(x)}{\partial Z_0 \partial V} = B\left[\int_0^{\infty} u e^{-Vu} K_1\left(\frac{\sqrt{(u+z_0)^2+x^2}}{L}\right)\left(\frac{u+z_0}{L\sqrt{(u+z_0)^2+x^2}}\right)du\right] \tag{A16}$$

$$\frac{\partial^2 u_{\text{model}}(x)}{\partial B \partial Z_0} = \left[\begin{array}{l} K_0\left(\frac{x}{L}\right) \\ -\int_{-z_0}^{0} K_1\left(\frac{\sqrt{(u+z_0)^2+x^2}}{L}\right)\left(\frac{u+z_0}{L\sqrt{(u+z_0)^2+x^2}}\right)du \\ -\int_0^{\infty} e^{-Vu} K_1\left(\frac{\sqrt{(u+z_0)^2+x^2}}{L}\right)\left(\frac{u+z_0}{L\sqrt{(u+z_0)^2+x^2}}\right)du \end{array}\right] \tag{A17}$$

$$\frac{\partial^2 u_{\text{model}}(x)}{\partial L \partial Z_0} = \left[\begin{array}{l} K_0\left(\frac{x}{L}\right)\left(\frac{x}{L^2}\right) \\ -\int_{-z_0}^{0} K_0\left(\frac{\sqrt{(u+z_0)^2+x^2}}{L}\right)\left(\frac{u+z_0}{L^3}\right)du \\ -\int_0^{\infty} e^{-Vu} K_0\left(\frac{\sqrt{(u+z_0)^2+x^2}}{L}\right)\left(\frac{u+z_0}{L^3}\right)du \end{array}\right] \tag{A18}$$

$$\frac{\partial^2 u_{\text{model}}(x)}{\partial V \partial Z_0} = B\left[\int_0^{\infty} u e^{-Vu} K_1\left(\frac{\sqrt{(u+z_0)^2+x^2}}{L}\right)\left(\frac{u+z_0}{L\sqrt{(u+z_0)^2+x^2}}\right)du\right] \tag{A19}$$

$$\frac{\partial^2 u_{\text{model}}(x)}{\partial {Z_0}^2} = B\left[\begin{array}{l} 2\int_{-z_0}^{0} K_1\left(\frac{\sqrt{(u+z_0)^2+x^2}}{L}\right)\left(\frac{(u+z_0)^2}{L\left[(u+z_0)^2+x^2\right]^{3/2}}\right)du \\ -\int_{-z_0}^{0} K_1\left(\frac{\sqrt{(u+z_0)^2+x^2}}{L}\right)\left(\frac{1}{L\sqrt{(u+z_0)^2+x^2}}\right)du \\ +\int_{-z_0}^{0} K_0\left(\frac{\sqrt{(u+z_0)^2+x^2}}{L}\right)\left(\frac{(u+z_0)^2}{L^2\left|(u+z_0)^2+x^2\right|}\right)du \\ +2\int_{0}^{\infty} e^{-Vu} K_1\left(\frac{\sqrt{(u+z_0)^2+x^2}}{L}\right)\left(\frac{(u+z_0)^2}{L\left[(u+z_0)^2+x^2\right]^{3/2}}\right)du \\ -\int_{0}^{\infty} e^{-Vu} K_1\left(\frac{\sqrt{(u+z_0)^2+x^2}}{L}\right)\left(\frac{1}{L\sqrt{(u+z_0)^2+x^2}}\right)du \\ +\int_{0}^{\infty} e^{-Vu} K_0\left(\frac{\sqrt{(u+z_0)^2+x^2}}{L}\right)\left(\frac{(u+z_0)^2}{L^2\left|(u+z_0)^2+x^2\right|}\right)du \end{array}\right] \quad \text{(A20)}$$

THIS PAGE INTENTIONALLY LEFT BLANK

LIST OF REFERENCES

[1] R. Mowatt-Larssen. (2010, Nov.). Al Qaeda's nuclear ambitions. *Foreign Policy* [Online]. Available: http://www.foreignpolicy.com/articles/2010/11/16/al_qaedas_nuclear_ambitions

[2] S. Tomlin. (2006, Mar.). The quest for a finer gamma ray detector. *Nature: International Weekly Journal of Science* [Online]. Available: http://www.nature.com/news/2006/060316/full/news060313-13.html.

[3] T.E. Schlesinger, J.E. Toney, H. Yoon, B.A. Brunett, L. Franks, and R.B. James, "Cadmium zinc telluride and its use as a nuclear radiation detector material," *Materials Sci. and Eng.: R: Reports*, vol. 32, no. 4-5, pp. 103–189, Apr. 2001.

[4] D. J. Phillips, "Transport imaging of spatial distribution of mobility-lifetime product in bulk semiconductors for nuclear radiation detection," Ph.D. dissertation, Dept. of Physics, Naval Postgraduate School, Monterey, CA, 2012.

[5] G. Yang, A.E. Bolotnikov, Y. Cui, G.S. Camarda, A. Hossain, and R.B. James, "Impurity gettering effect of Te inclusions in CdZnTe single crystals," *Journal of Crystal Growth*, vol. 311, no. 1, pp. 99–102, Oct. 2008.

[6] J.R. Heffelfinger, D.L. Medlin, and R.B. James, "Cadmium zinc telluride and its use as a nuclear radiation detector material," *MRS Proc.*, vol. 484, no. 247, pp. 40–50, Mar. 1998.

[7] D. Henry. (2012, May.). Electron-sample interactions. [Online]. Available: http://serc.carleton.edu/research_education/geochemsheets/electroninteractions.html

[8] K. E. Blaine, "Contact-free measurement of mobility-lifetime product using transport imaging," *M.S. Thesis*, Dept. of Physics. Naval Postgraduate School, Monterey, CA, 2011.

[9] K. E. Blaine, D. J. Phillips, C. L. Frenzen, C. Scandrett, and N. M. Haegel, "Three-dimensional transport imaging for the spatially-resolved determination of carrier diffusion length in bulk materials," *Rev. Sci. Instrum.*, vol. 83, pp. 043702-1–043702-7, 2012.

[10] ASPEX Corporation. (2013, Mar.), Energy Dispersive X-Ray Spectroscopy. [Online]. Available: http://www.aspexcorp.com/solutions/omegamax/edxspectroscopy.aspx.

[11] Failure Analysis Site. (2012, Oct.). “Knock Atoms Off by FIB.” [Online]. Available: http://handchat-castle3-euig7arc.blogspot.com/2012/10/contributor-r-carpenter-knock-atoms-off.html.

[12] C. Kittel, *Introduction to Solid State Physics*, New York: John Wiley and Sons, 1996.

[13] R. Grill, J. Franc, E. Belas, P. Höschl, B. Nahlovskyy, P.Moravec, P. Fochuk, Y. Verzhak, and O. Panchuck, “Dynamics of point defects in tellurium-rich CdTe,” *IEEE Trans. on Nucl. Sci.*, vol. 54, no. 4, Aug. 2007.

[14] B.C. Yacobi and D.B. Holt, *Cathodoluminescence Microscopy of Inorganic Solids*, New York: Plenum Press, 1990.

[15] T. E. Everhart and P. H. Hoff, “Determination of kilovolt electron energy dissipation vs. penetration distance in solid materials,” *J. Phys. D: Appl. Phys.*, vol. 42, no. 13, Oct. 1971.

[16] K. Kanaya and S. Okayama, “Penetration and energy-loss theory of electrons in solid targets,” *J. Phys. D: Appl. Phys.*, vol. 5, no. 43, Oct. 1972.

INITIAL DISTRIBUTION LIST

1. Defense Technical Information Center
   Ft. Belvoir, Virginia

2. Dudley Knox Library
   Naval Postgraduate School
   Monterey, California